

Single-shot parity readout of a minimal Kitaev chain

Nick van Loo^{1*†}, Francesco Zatelli^{1†}, Gorm O. Steffensen^{2†}, Bart Roovers^{1†},
 Guanzhong Wang¹, Thomas Van Caekenberghe¹, Alberto Bordin¹, David
 van Driel¹, Yining Zhang¹, Wietze D. Huisman¹, Ghada Badawy³,
 Erik P.A.M. Bakkers³, Grzegorz P. Mazur¹, Ramón Aguado²,
 Leo P. Kouwenhoven^{1*}

¹QuTech and Kavli Institute of Nanoscience, Delft University of Technology,
 The Netherlands.

²Instituto de Ciencia de Materiales de Madrid (ICMM),
 Consejo Superior de Investigaciones Científicas (CSIC), Spain.

³Department of Applied Physics, Eindhoven University of Technology,
 The Netherlands.

*Corresponding author(s). E-mail(s): n.vanloo@tudelft.nl; l.p.kouwenhoven@tudelft.nl;

[†]These authors contributed equally to this work.

Abstract

Protecting qubits from noise is essential for building reliable quantum computers. Topological qubits offer a route to this goal by encoding quantum information non-locally, using pairs of Majorana zero modes. These modes form a shared fermionic state whose occupation – either even or odd – defines the fermionic parity that encodes the qubit. Crucially, this parity cannot be accessed by any measurement that probes only one Majorana mode. This reflects the non-local nature of the encoding and its inherent protection against noise. A promising platform for realizing such qubits is the Kitaev chain, implemented in quantum dots coupled via superconductors. Even a minimal chain of two dots can host a pair of Majorana modes and store quantum information in their joint parity. Here we introduce a new technique for reading out this parity, based on quantum capacitance. This global probe senses the joint state of the chain and enables real-time, single-shot discrimination of the parity state. By comparing with simultaneous local charge sensing, we confirm that only the global signal resolves the parity. We observe random telegraph switching and extract parity lifetimes exceeding one millisecond. These results establish the essential readout step for time-domain control of Majorana qubits, resolving a long-standing experimental challenge.

Introduction

In the quest for fault-tolerant quantum computing, Majorana zero modes (MZMs) are promising quantum states to encode a topological qubit that is intrinsically protected against noise [1–4]. One of the simplest theoretical models supporting MZMs is the Kitaev chain: a one-dimensional array of spinless fermionic sites with superconducting pairing [1]. The recent realization of such chains in quantum dots (QDs) coupled via superconductors has opened an exciting new frontier [5, 6]. Interestingly, the minimal version of these chains already hosts a pair of MZMs at a fine-tuned sweet spot [7, 8]. These states, often referred to as “poor man’s Majoranas”, lack topological protection but retain essential features such as non-locality and non-Abelian statistics [9–12]. As such, they offer a promising testbed for Majorana-based quantum operations.

In the minimal chain, each MZM γ_1 and γ_2 is localized on a different quantum dot. Together, they form a non-local fermion $c = (\gamma_1 + i\gamma_2)/\sqrt{2}$, which stores quantum information in its fermionic parity. The corresponding parity operator $P_{12} = i\gamma_1\gamma_2$ reflects this non-local encoding and is the key observable for qubit readout and measurement-based protocols [11, 13–15]. Crucially, any readout must couple to both MZMs to access this parity (Fig. 1a) [1, 14–16]. In contrast, a local probe that couples to only one mode cannot distinguish between parity states (Fig. 1b). This measurement constraint is not incidental – it reflects the non-local encoding of quantum information and its inherent protection against local noise. In the context of minimal Kitaev chains, theory predicts that local charge sensing is insensitive to parity, while global probes that detect charge fluctuations can resolve it [8].

The non-local encoding ensures that the parity state is robust against local perturbations, but only as long as the total fermionic parity is conserved. In practice, this conservation can be broken by quasiparticles entering the device, a process known as quasiparticle poisoning. This causes a Majorana qubit to leak out of the computational subspace, destroying the stored quantum information [17]. Similar poisoning limits the performance of superconducting and hybrid qubits [18–20]. Characterizing parity lifetimes and achieving high-fidelity parity readout are thus essential steps toward Majorana-based qubits and topological quantum computing [17, 21, 22].

In this work, we introduce a measurement technique that distinguishes the fermionic parity of a minimal Kitaev chain through its global quantum capacitance [9, 23]. By comparing to simultaneous local charge sensing, we show that only the global probe distinguishes the parity states. This enables real-time detection of parity switching and highlights the non-local nature of the underlying Majorana modes.

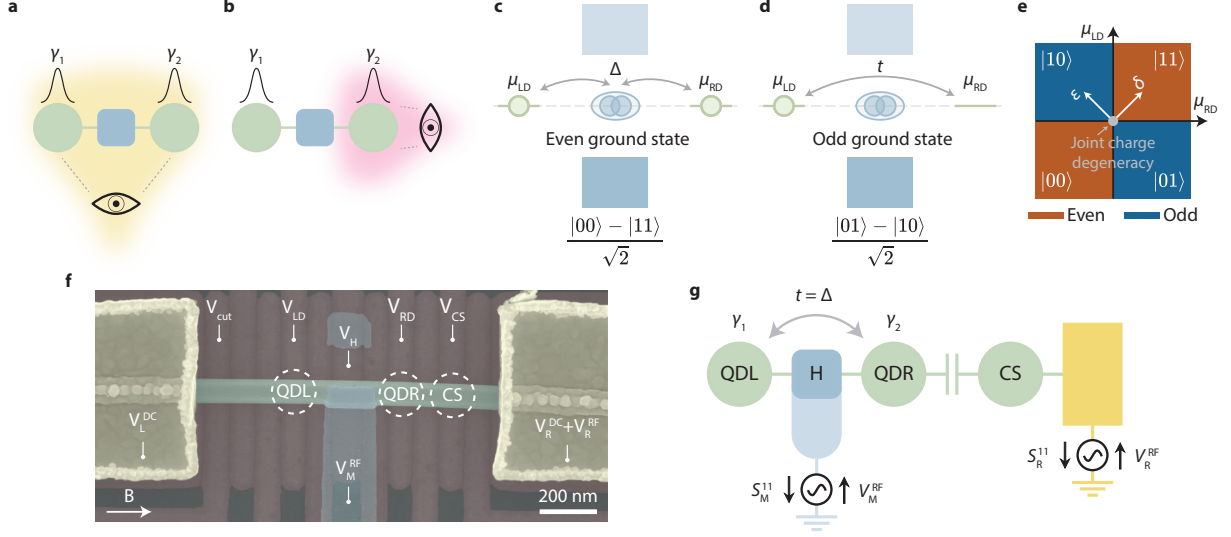


Fig. 1 Minimal Kitaev chain and parity measurement setup. **a**, Illustration of a global parity measurement, coupling simultaneously to both Majorana zero modes γ_1 and γ_2 . **b**, Illustration of a local measurement that couples only to one Majorana mode, and cannot distinguish parity states. **c**, Energy diagram of the even parity sector, where $|00\rangle$ and $|11\rangle$ hybridize via crossed Andreev reflection (CAR) in the superconductor. **d**, Energy diagram of the odd parity sector, where $|10\rangle$ and $|01\rangle$ hybridize via elastic co-tunneling (ECT). **e**, Charge-stability diagram of two quantum dots with chemical potentials μ_{LD} and μ_{RD} , showing the detuning axis ε and common-mode axis δ . Orange and blue sectors denote the even and odd parity ground states. The center marks the joint charge degeneracy, which is the Majorana sweet spot when $t = \Delta$. **f**, False-colored scanning electron micrograph of the device. The InSb nanowire (green) is proximitized by an Al strip (blue) and contacted by Cr/Au leads (yellow). Quantum dots (dashed circles) are defined using Ti/Pd bottom gates (red). The Kitaev chain is tuned by V_{LD} , V_{RD} and V_H . The device is isolated from the left lead using V_{cut} . The charge sensor (CS) is controlled with V_{CS} and the nanowire is depleted between QDR and CS. **g**, Schematic of the readout setup. The two QDs are coupled through a superconducting segment connected to an RF resonator, for global readout via S_M^{11} . Likewise, the CS is read out via a second resonator S_R^{11} .

Quantum capacitance of the minimal Kitaev chain

A minimal Kitaev chain consists of two spinless fermionic sites with on-site energies μ_{LD} and μ_{RD} . The sites are coupled by elastic co-tunneling (ECT) and crossed Andreev reflection (CAR), with amplitudes t and Δ , respectively. Each site can be either occupied or empty, giving rise to four charge configurations $|n_{LD}n_{RD}\rangle$, where $n_{LD}, n_{RD} \in \{0, 1\}$. At charge degeneracy, the even states $|00\rangle$ and $|11\rangle$ hybridize via CAR to form bonding and anti-bonding combinations $|e\rangle = (|00\rangle \pm |11\rangle)/\sqrt{2}$ (Fig. 1c). Likewise, the odd states $|10\rangle$ and $|01\rangle$ hybridize via ECT to form $|o\rangle = (|10\rangle \pm |01\rangle)/\sqrt{2}$ (Fig. 1d). These define two parity branches with distinct energy dispersions:

$$E_e^\pm = \delta \pm \sqrt{\delta^2 + \Delta^2}, \quad (1)$$

$$E_o^\pm = \delta \pm \sqrt{\varepsilon^2 + t^2}. \quad (2)$$

Here, E_e^\pm and E_o^\pm are the even and odd eigenenergies with \pm denoting ground and excited states, $\varepsilon = (\mu_{LD} - \mu_{RD})/2$ defines the detuning axis and $\delta = (\mu_{LD} + \mu_{RD})/2$ the common-mode axis. When $t = \Delta$ and $\mu_{LD} = \mu_{RD} = 0$, the two ground states become degenerate, giving rise to zero-energy excitations

with Majorana character on each dot [8]. The corresponding charge-stability diagram is shown in Fig. 1e, where the Majorana sweet spot is located at the joint charge degeneracy.

Our realization of this model (Fig. 1f) consists of an InSb nanowire [24] contacted by an Al film and two Cr/Au leads. The Al film induces superconductivity in the wire, forming a short hybrid segment. Both the superconductor and right lead connect to multiplexed LC resonators [25], allowing RF reflectometry via V_M^{RF} and V_R^{RF} at resonance frequencies $f_M \approx 340.8$ MHz and $f_R \approx 704.0$ MHz. The superconductor is grounded via a bias tee and serves as a global probe, while DC bias voltages V_L^{DC} and V_R^{DC} can be applied to the normal contacts. Electrostatic confinement is controlled by Ti/Pd gates separated by an $\text{Al}_2\text{O}_3/\text{HfO}_2$ dielectric layer. Two quantum dots (QDL and QDR) are formed adjacent to the hybrid segment to implement the Kitaev chain. A third dot acts as a single-lead charge sensor (CS) [26–28], coupled only capacitively to QDR. Their electrochemical potentials are controlled by V_{LD} , V_{RD} and V_{CS} . A parallel magnetic field $B = 150$ mT ensures spin polarization of the QDs [5]. The coupling between QDL and QDR is mediated by Andreev bound states. Crucially, the CAR and ECT strengths depend on the electrochemical potential of these states and can be made equal through tuning V_{H} [5]. Additional information on the experimental setup and nanofabrication can be found in Methods sections I and II, Fig. ED1 and Fig. ED2.

Setting up the Kitaev chain is typically done using transport measurements [5], which require coupling to normal leads. However, this continuously injects quasiparticles and changes fermion parity, preventing quantum information applications. To preserve parity, we isolate the device from the normal contacts by depleting the nanowire with V_{cut} (Fig. 1f). To measure the isolated system, we have two readout tools at our disposal as depicted schematically in Fig. 1g: the reflected signal S_R^{11} from the charge sensor, and S_M^{11} from the resonator coupled to both quantum dots via the superconducting lead. We analyze these signals projected along their principal axes as ΔS_R^{11} and ΔS_M^{11} (see Methods section II).

We first focus on the superconducting lead. The applied RF signal induces small oscillations in its electrochemical potential relative to the QDs, effectively modulating the system along the common-mode axis δ . As seen from Eqs. 1 and 2, this reveals a key difference between the parity branches: even states disperse nonlinearly due to hybridization via CAR, while the odd states change linearly (Fig. 2a). This is reflected in the curvature of their energy levels and thus in their quantum capacitance, which is proportional to the second derivative of energy with respect to chemical potential (see Methods section VI). Intuitively, the RF oscillation periodically shifts the balance between $|00\rangle$ and $|11\rangle$, inducing charge motion between the quantum dots and the superconductor and producing a measurable quantum capacitance. In contrast, the odd states $|01\rangle$ and $|10\rangle$ are connected by tunneling that does not involve net charge transfer to or from the superconductor, yielding zero quantum capacitance. This behavior appears in Fig. 2b, where only the even state has a finite signal near $\delta = 0$. In addition, the contrast between even

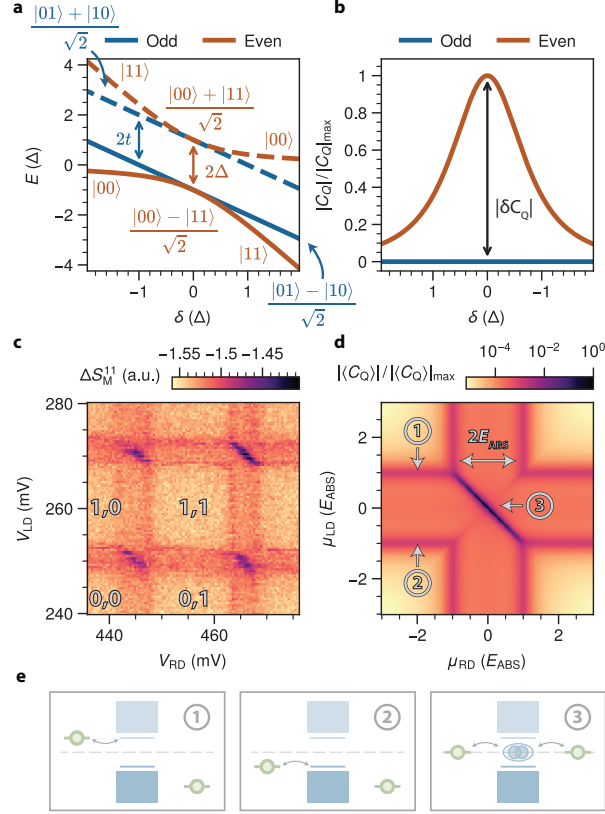


Fig. 2 Quantum capacitance of the chain. **a**, Energy dispersion of the even (CAR-coupled) and odd (ECT-coupled) parity states at zero detuning ($\varepsilon = 0$), plotted as a function of the common-mode potential δ along which V_M^{RF} is applied. **b**, Calculated quantum capacitance for each parity branch, given by the second derivative of energy with respect to chemical potential. A strong contrast appears near the degeneracy point where even states show maximal curvature. **c**, Charge-stability diagram with labeled charge states measured via the global quantum capacitance signal ΔS_M^{11} . The dominant anti-diagonal lines correspond to $\mu_{LD} = -\mu_{RD}$, where the strength of CAR is maximal. **d**, Simulation of the quantum capacitance around one charge degeneracy (see Methods section VI), showing features consistent with the experiment. **e**, Energy diagrams of the relevant hybridization processes. (1) and (2) correspond to hybridization between a single dot and the lowest-energy state in the hybrid segment; (3) shows interdot hybridization at joint charge degeneracy.

and odd parity states reaches a maximum at this point which scales as $\delta C_Q \propto \Delta^{-1}$ [9]. The resulting parity-dependent frequency shift of the resonator is detected in ΔS_M , providing a superconducting analog to reflectometry-based sensing in conventional double dots [29]. Here, however, the signal arises from Cooper-pair splitting rather than interdot tunneling.

Figure 2c shows a measurement of ΔS_M^{11} as the chemical potentials of the two QDs are varied, with weak interdot coupling. The most prominent feature is a strong anti-diagonal line through the joint charge degeneracies, where $|00\rangle$ and $|11\rangle$ form equal superposition and the total charge is most susceptible to variations of δ . This results in a pronounced signal that we attribute to quantum capacitance, in agreement with Fig. 2b. Additional horizontal and vertical bands appear when only one QD is near resonance. These arise from hybridization between a single dot level and the lowest-energy state in the hybrid segment, generating finite quantum capacitance without interdot coupling. Their widths reflect the energy of this state E_{ABS} , with maximum signal at resonance. Our theoretical model (Fig. 2d; see Methods section VI) qualitatively reproduces these features, treating the hybrid segment as a spinful resonant level coupled

to a superconductor in the presence of spin-orbit coupling. The energy diagrams in Fig. 2e illustrate the processes behind the observed signals. The band visibility depends on QD-hybrid coupling strength, while the joint resonance signal reflects interdot coupling. Figure ED3 shows how tuning V_H modifies this behavior. These features help identify suitable joint degeneracies for time-domain parity readout, as discussed next.

Time-resolved parity measurements

We tune the device to a configuration with strong interdot coupling via transport measurements to locate regions where Majorana sweet spots are expected (see Methods section III). We then isolate the device from the left lead using V_{cut} and track the relevant quantum dot resonances while compensating for cross-capacitance. In Fig. 3, we focus on quantum capacitance measurements as schematically depicted in Fig. 3a. The corresponding charge-stability diagram is shown in Fig. 3b. At the center where both dots are on resonance ($\mu_{\text{LD}} = \mu_{\text{RD}} = 0$), we record a time trace of ΔS_M^{11} , which shows discrete switching between two values (Fig. 3c). These switching events reflect transitions between parity ground states of the system. A two-state hidden Markov model (see Methods section IV) identifies these transitions and yields a characteristic switching time $\tau_{\text{avg}} = 1.85 \pm 0.03$ ms. The histogram (Fig. 3d) shows a clear bimodal

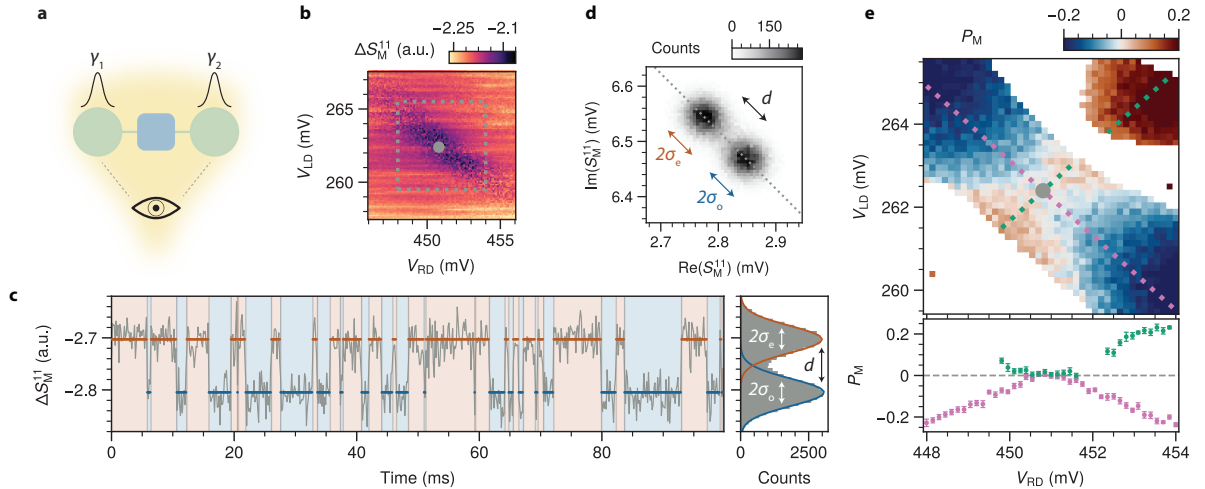


Fig. 3 Time-resolved parity switching via quantum capacitance **a**, Illustration of the quantum capacitance readout that couples to both MZMs and constitutes a global measurement. **b**, Charge-stability diagram of QDL and QDR measured through ΔS_M^{11} . Random telegraph noise near the anti-diagonal resonance reflects real-time parity switching. **c**, Time trace of ΔS_M^{11} recorded near the center of the charge-stability diagram ($V_{\text{LD}} = 262.4$ mV and $V_{\text{RD}} = 450.8$ mV, shown as a gray dot in panels **b** and **e**), showing discrete switching events between parity states. For this trace, an integration time of 150 μ s is used which yields $\text{SNR}_M = 1.958 \pm 0.006$ and readout error of 6%. States are assigned and highlighted in color using a hidden Markov model, which yields $\tau_e = 1.82 \pm 0.05$ ms, $\tau_o = 1.88 \pm 0.04$ ms. The side panel displays count histograms along the principal component axis. Methods for data acquisition and analysis are described in section IV. **d**, Histogram of complex S_M^{11} from the time trace in panel **c**. The separation d and standard deviation σ_e and σ_o of the distributions are used to calculate the signal-to-noise ratio $\text{SNR} = d/(\sigma_e + \sigma_o)$. The dotted line indicates the principal component axis along which the data is projected. **e**, Top: Map of parity polarization P_M around the joint charge degeneracy inside the dotted gray box of panel **b**, derived from 10 s time traces. Only pixels for which $\text{SNR}_M \geq 0.5$ are included (see also Methods section IV and Fig. ED5). Bottom: Line cuts of P_M along the diagonal (green) and anti-diagonal (pink) directions in the top panel, showing approximately quadratic dependence consistent with energy detuning from the sweet spot.

distribution, corresponding to the even and odd parity ground states. The absence of the excited states in this figure suggests fast relaxation to the ground state within each parity sector, consistent with reported nanosecond timescales for double quantum dots [30]. By varying the integration time, we optimize the signal-to-noise ratio (SNR_M) and readout error (see Fig. ED4). This yields a single-shot readout time of $40\text{ }\mu\text{s}$ for $\text{SNR}_M = 1$, and an optimal integration time of $150\text{ }\mu\text{s}$ with a minimal readout error of 6 %.

To gain further insight into the system’s dynamics, we analyze time traces of the resonator signal to extract the lifetimes τ_e and τ_o of the even and odd parity states. From these, we compute the parity polarization $P_M = (\tau_e - \tau_o)/(\tau_e + \tau_o)$. This quantity indicates the probability of finding the system in either parity state: near zero implies both are equally likely, while positive or negative values signal an imbalance. We measure P_M across a grid of chemical potentials around the joint charge degeneracy (dotted gray box in Fig. 3b), producing the map shown in Fig. 3e. The polarization varies with dot energies, reaching near-zero at the center where dot levels align. Line cuts along the diagonal and anti-diagonal directions show a quadratic variation near the center, consistent with previous observations in minimal Kitaev chains where the energy splitting grows quadratically upon detuning. This behavior can be understood by modeling the system as coupled to a hot reservoir of fermions [31, 32] (see Methods section VI). In this model, the system switches between parity states with rates that depend on their energy. The state with lower energy lives longer, so the observed polarization reflects the energy difference between the two states. We also observe a secondary polarization feature in the upper-right of the map, arising from hybridization in the odd parity sector with a state in the hybrid segment (see Methods VI).

We test the robustness of this approach by varying V_H , which tunes the CAR and ECT strengths between the dots. As shown in Fig. ED5, the shape of the polarization region evolves with V_H , resembling the transition between CAR and ECT observed in transport measurements. This suggests that polarization mapping can indicate sweet spot conditions even when the device is isolated. For Fig. 3, we chose $V_H = 1.665\text{ V}$, where the polarization approaches zero near the center of the charge-stability diagram, consistent with a Majorana sweet spot. Transport measurements after reconnecting the left lead confirm a sweet spot nearby, at $V_H = 1.675\text{ V}$ (Fig. ED6).

Local indistinguishability of Majorana zero modes

We next compare two complementary measurements of the Kitaev chain: quantum capacitance readout via the superconducting lead and local charge sensing via a nearby quantum dot (characterized in Fig. ED7). These methods probe different aspects of the system: the charge sensor detects local changes in the charge on one quantum dot, while quantum capacitance measures how easily charge flows between the dots and the superconductor. This global response depends on the combined state of both dots and is sensitive to their shared parity. Time traces of both signals were recorded simultaneously, as illustrated in Fig. 4a.

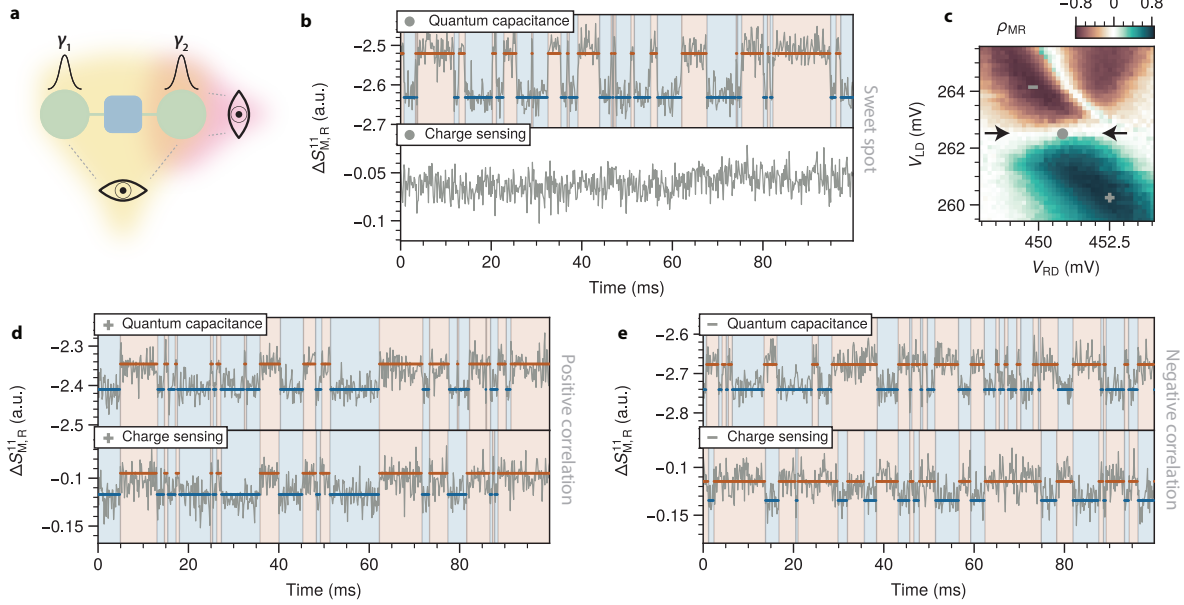


Fig. 4 Local and global probes of parity switching. **a**, Schematic of the dual readout setup: global parity is detected via quantum capacitance ΔS_M^{11} and local charge via a nearby charge sensor ΔS_R^{11} . **b**, Time traces recorded near the sweet spot (gray dot in panel c, $V_{LD} = 262.5$ mV and $V_{RD} = 450.8$ mV). Parity switching is observed only in the quantum capacitance signal, indicating local indistinguishability of the parity states ($\rho_{MR} \approx 0.03$). **c**, Map of the Pearson correlation coefficient ρ_{MR} across the charge-stability diagram of QDL and QDR, calculated between the state assignment of the two signals. The correlation vanishes near a horizontal line highlighted by black arrows ($V_{LD} = 262.5$ mV), indicating $t \approx \Delta$. **d**, Time traces recorded away from degeneracy (gray plus in panel b), where both signals resolve switching events with strong correlation ($\rho_{MR} \approx 0.85$). **e**, Time traces in the anti-correlated regime (gray minus in panel b). Switching appears in both signals but with opposite sign, reflecting a global parity inversion with no local charge change ($\rho_{MR} \approx -0.81$).

Near the center of the charge-stability diagram, parity switching appears only in the quantum capacitance signal (Fig. 4b). The charge sensor remains insensitive because it couples to just one MZM and cannot detect their shared parity, whereas the superconductor couples to both and probes the system as a whole. At charge degeneracy, the even and odd parity states carry equal average charge on QDR, making them locally indistinguishable. This remains true independent of the relative strength of the CAR and ECT couplings.

Detuning the dot potentials away from charge degeneracy breaks the balance between the even and odd states. Their charge distributions shift, leading to different average charge on QDR. As a result, the charge sensor becomes sensitive to the parity state. In this regime, both the quantum capacitance and charge sensor detect switching events (Fig. 4d). Their signals are strongly correlated, meaning both sensors detect the same transitions. We quantify this using the Pearson correlation coefficient $\rho_{MR} \approx 0.85$, where $\rho_{MR} = +1$ indicates perfect correlation and $\rho_{MR} = -1$ perfect anti-correlation. We attribute imperfect correlations and anti-correlations to the limited SNR that results from operating both sensors outside their optimal sensitivity regimes (see Methods section IV).

Figure 4c shows a full map of the correlation coefficient, which is strongest where both sensors clearly detect parity switching. Interestingly, the sign of the correlation flips between the top and bottom halves

of the map. This occurs because the global parity ground state changes as QDL crosses a charge transition. The quantum capacitance reflects this change, since it senses the combined state of both dots, while the charge sensor responds only to local charge on QDR. As a result, the two measurements respond in opposite ways to the same parity-switching events, leading to anti-correlation (Fig. 4e). This sign flip illustrates the non-local character of the parity state: tuning one dot affects the overall parity without altering the charge on the other.

At the center of the charge-stability diagram, the correlation coefficient crosses through zero. Here, the charge sensor becomes insensitive to the parity state because both parity branches produce the same average charge on QDR. In this situation, switching between even and odd states no longer causes a detectable change in the local signal. We predict that this condition occurs along the line $\mu_{LD} = \frac{\Delta-t}{\Delta+t} \mu_{RD}$, which becomes horizontal ($\mu_{LD} = 0$) at the Majorana sweet spot ($t = \Delta$), as explained in detail in Methods section VI. In our data, the zero-correlation line (black arrows in Fig. 4c) aligns with this prediction. At other V_H values, the line tilts, consistent with detuning from the sweet spot. In addition, the width of this line reflects the strength of the couplings and, by extension, the gap to the excited states of the chain (see Fig. ED5, Fig. ED8 and Fig. ED9 for experimental examples and Methods section VI and Fig. ED10 for theory).

These results demonstrate that quantum capacitance and charge sensing offer complementary perspectives on the Kitaev chain. While quantum capacitance captures the global parity, charge sensing measures only the local charge of the two parity states. Since these are highly entangled states, the local measurement is insufficient to distinguish them near the sweet spot, where the parity branches produce the same local charge. Their combined use provides a consistent picture of parity in minimal Kitaev chains and establishes global quantum capacitance as a powerful tool for its readout.

Discussion and conclusion

To implement parity readout in a minimal Kitaev chain, we combined complementary measurement strategies of charge sensing, parity polarization, and transport to guide device tuning. These tools consistently indicate operation near the Majorana sweet spot. Crucially, the readout does not rely on precise tuning: the quantum capacitance remains sensitive to fermionic parity even away from exact degeneracy. In future qubit implementations, any residual energy splitting $E_M = |t - \Delta|$ will manifest as coherent parity oscillations, allowing optimal fine-tuning via Ramsey-type spectroscopy [11, 33, 34].

The readout technique introduced here is designed for integration into qubit architectures. In the envisioned geometry of two Kitaev chains connected via a shared superconductor, each chain contributes a parity-dependent quantum capacitance. This enables the single-shot discrimination of all four parity states, allowing to detect leakage out of the computational subspace [34]. The method extends to longer

chains: via base-band pulses on the quantum dots so that only two remain resonant during readout, the chain can be effectively reduced to a minimal configuration without disturbing the encoded state. Additionally, we observe that the resonator drive can bias the parity distribution (Fig. ED4a,b), suggesting a path toward parity initialization via dynamical polarization [35].

This work overcomes a key challenge in realizing Majorana-based qubits by enabling fast, high-fidelity parity readout. While similar functionality has recently been demonstrated using interferometric techniques in extended hybrid devices [22], those approaches require significant alterations to the device layout and introduce considerable control overhead. In contrast, our method integrates seamlessly with existing device elements, enabling parity readout without added operational complexity. Additionally, the simultaneous use of a charge sensor allows us to verify the local charge-neutrality of the parity states, a key signature of Majorana modes that cannot be accessed in interferometric geometries. With this capability in place, gate-based control methods established in spin qubits become directly applicable. This positions the minimal Kitaev chain as a fully operational platform for time-domain experiments on Majorana fusion, braiding, and computation.

Data Availability and Code Availability

The raw data measured on the device presented in this work, the data processing and plotting code, and the code used for the theory calculations are available at <https://doi.org/10.4121/227fd419-fded-4a96-ab62-421a0cd57fa5>.

Acknowledgements

This work has been supported by the Dutch Organization for Scientific Research (NWO), Microsoft Corporation Station Q, the Spanish Ministry of Science (grant No. PID2021-125343NB-I00) and the Horizon Europe Framework Program of the European Commission through the European Innovation Council Pathfinder Grant No. 101115315 (QuKiT). We thank O.W.B. Benningshof and J.D. Mensingh for technical assistance with the cryogenic electronics. We thank F.K. Malinowski for contributing to design of the experiment. We thank C.X. Liu and S.L.D. ten Haaf for their input on the manuscript. We thank T. Dvir, A. Lombardi, V.P.M. Sietses, F.J. Bennebroek Evertsz', M. Wimmer, J.D. Torres Luna, S. Miles, S. Goswami, S. Roelofs and D. Joshi for fruitful discussions. We thank J.M. Hornibrook and D.J. Reilly for providing the frequency multiplexing chips. We thank S. Gazibegovic for contribution to nanowire growth.

Author contributions

The sample was fabricated by N.v.L. and B.R. Measurements were performed by N.v.L., F.Z. and T.V.C. The experiment was designed by N.v.L., F.Z. and G.W. The data was analyzed by N.v.L. and F.Z. The experimental setup was designed and implemented by N.v.L., F.Z., B.R., G.W., and D.v.D. The manuscript was prepared by N.v.L. and F.Z. with input from all authors. G.W., A.B., D.v.D., Y.Z., W.D.H. and G.P.M. contributed to understanding and interpretation of the data through regular discussions. The project was supervised by L.P.K. Modeling and simulations of the system were done by G.O.S. and R.A. The InSb nanowire growth was performed by G.B. and E.P.A.M.B.

Competing interests

The authors declare no competing interests.

Extended data

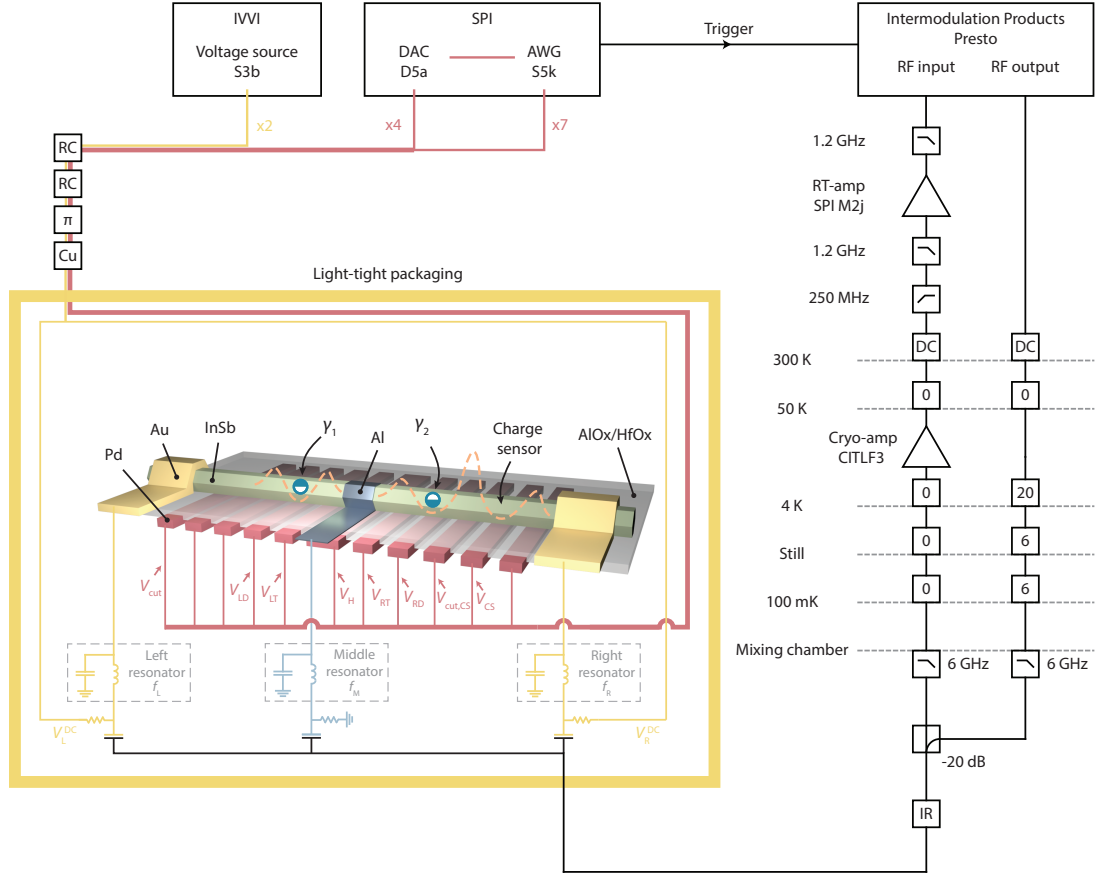


Fig. ED1 Measurement setup. Detailed wiring diagram for the DC and RF lines used to measure the device. To reduce the generation of non-equilibrium quasiparticles in the superconducting film we use IR filters for the RF lines. Additionally, light-tight packaging encloses the device. Finally, we note that an additional resonator was connected to the left normal lead, but it was not used.

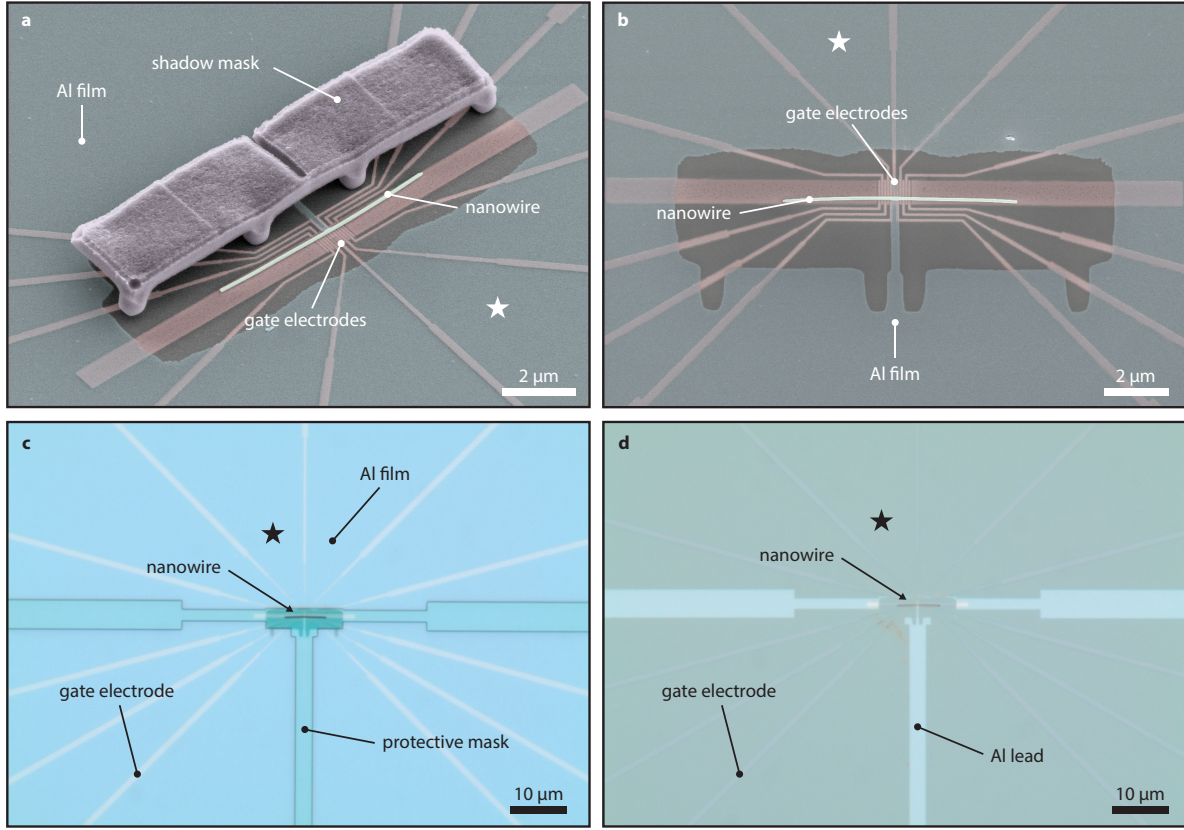


Fig. ED2 Shadow lithography with masks grown on-chip. **a**, False-colored tilted scanning electron micrograph of a nanowire (InSb, shown in green) on top of the gate electrode array (Pd, shown in red) after deposition of the superconductor (Al, shown in blue). The shadow mask (HSQ, shown in purple) has a narrow slit in the center through which the Al strip that contacts the nanowire is evaporated, at an angle of 30° with respect to the substrate. A star is placed at approximately the same location in this and the next panels to help identify the orientation of the substrate. **b**, False-colored top-view scanning electron micrograph of the same nanowire as in panel **a**, after the shadow mask has been mechanically removed using a nanomanipulator. **c**, Optical image of the PMMA mask which covers the nanowire and three leads towards the device. Image taken after patterning and development of the mask, but before etching of the Al film using Transene type D. **d**, Optical image of the device after etching of the Al film and stripping of the protective mask. The central Al lead connects the nanowire to a W pad which facilitates wire bonding (not shown here).

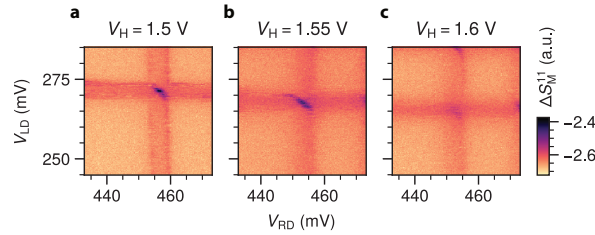


Fig. ED3 Evolution of quantum capacitance with hybrid gate voltage V_H **a–c** Quantum capacitance charge-stability diagrams measured using the middle resonator while the device is isolated from the normal leads. Each panel corresponds to a different setting of the hybrid gate voltage V_H , which tunes the energy of the Andreev bound state in the superconducting segment. As V_H increases, we observe a progressive weakening of the signal along the interdot detuning axis. This behavior is attributed to an increase in the strength of CAR between the quantum dots, mediated by the lowering of the Andreev bound state energy. Since quantum capacitance is inversely proportional to CAR strength, a stronger CAR leads to reduced signal contrast. This trend provides a qualitative probe of the CAR amplitude and helps identify regions where $t \approx \Delta$, as required for the Majorana sweet spot.

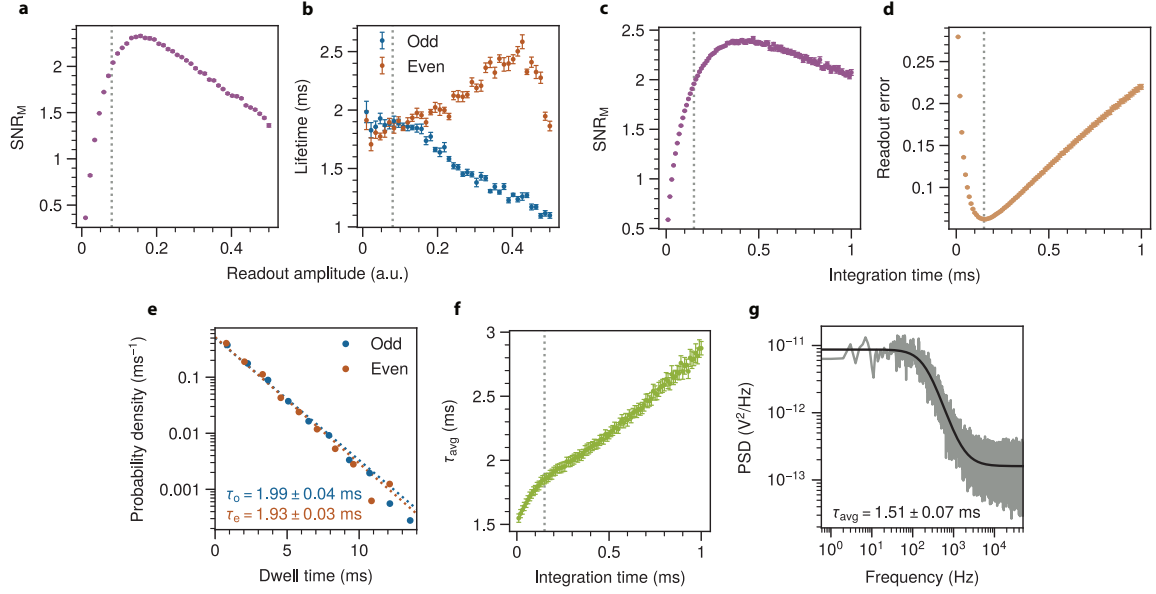


Fig. ED4 Detailed analysis of time-trace performance at the Majorana sweet spot. **a,b**, Signal-to-noise ratio (SNR_M , panel **a**) and parity lifetimes (panel **b**) as a function of readout amplitude. All data were taken with the same gate settings and $150\ \mu\text{s}$ integration time as in Fig. 3d. The gray dotted line indicates the amplitude used for Fig. 3 and Fig. 4. Beyond a certain readout amplitude, the SNR decreases and the lifetimes become amplitude-dependent, suggesting drive-induced backaction. This observation suggests that the system can be initialized in the even state by driving the middle resonator with a high amplitude. The time traces in panels **a,b** were averaged in time bins of $160\ \mu\text{s}$ (instead of $150\ \mu\text{s}$) to ensure that the averaging time is an exact multiple of the sampling rate ($50\ \text{kHz}$). **c,d**, SNR_M (**c**) and readout error (**d**) of the time trace presented in Fig. 3 versus integration time. The readout error was estimated as $\left[1 - e^{-\tau_{\text{bin}}/\tau_{\text{avg}}} \text{erf}(\text{SNR}_M(\tau_{\text{bin}})/\sqrt{2})\right]/2$ [22], where τ_{bin} is the integration time and $\tau_{\text{avg}} = 1.85 \pm 0.03\ \text{ms}$. The gray dotted line indicates the integration time $\tau_{\text{bin}} = 150\ \mu\text{s}$ used for all the reported measurements unless otherwise specified. **e**, Histograms of dwell times in the even and odd parity states, normalized by total counts. The dotted lines show fits with the corresponding Poissonian probability densities $e^{-t/\tau_{o,e}}/\tau_{o,e}$, confirming that the dwell times follow an exponential distribution. $\tau_{o,e}$ have been estimated as the mean of the dwell times in the odd and even parity state. Their uncertainty has been estimated as the standard deviation of the mean. **f**, Average switching time, τ_{avg} , estimated for varying integration time. As the integration time increases, the estimation of τ_{avg} is systematically biased towards higher values. See Methods section IV for a more detailed discussion. **g**, Power spectral density (PSD) of the time trace using an integration time of $10\ \mu\text{s}$. By fitting it with a Lorentzian model, we extract an average switching time of $1.51 \pm 0.07\ \text{ms}$. The discrepancy between this estimate and those obtained with a hidden Markov model or exponential fitting further suggests that the long integration time needed to obtain high SNR could systematically bias the estimation of τ_{avg} . See Methods section IV for a more detailed discussion.

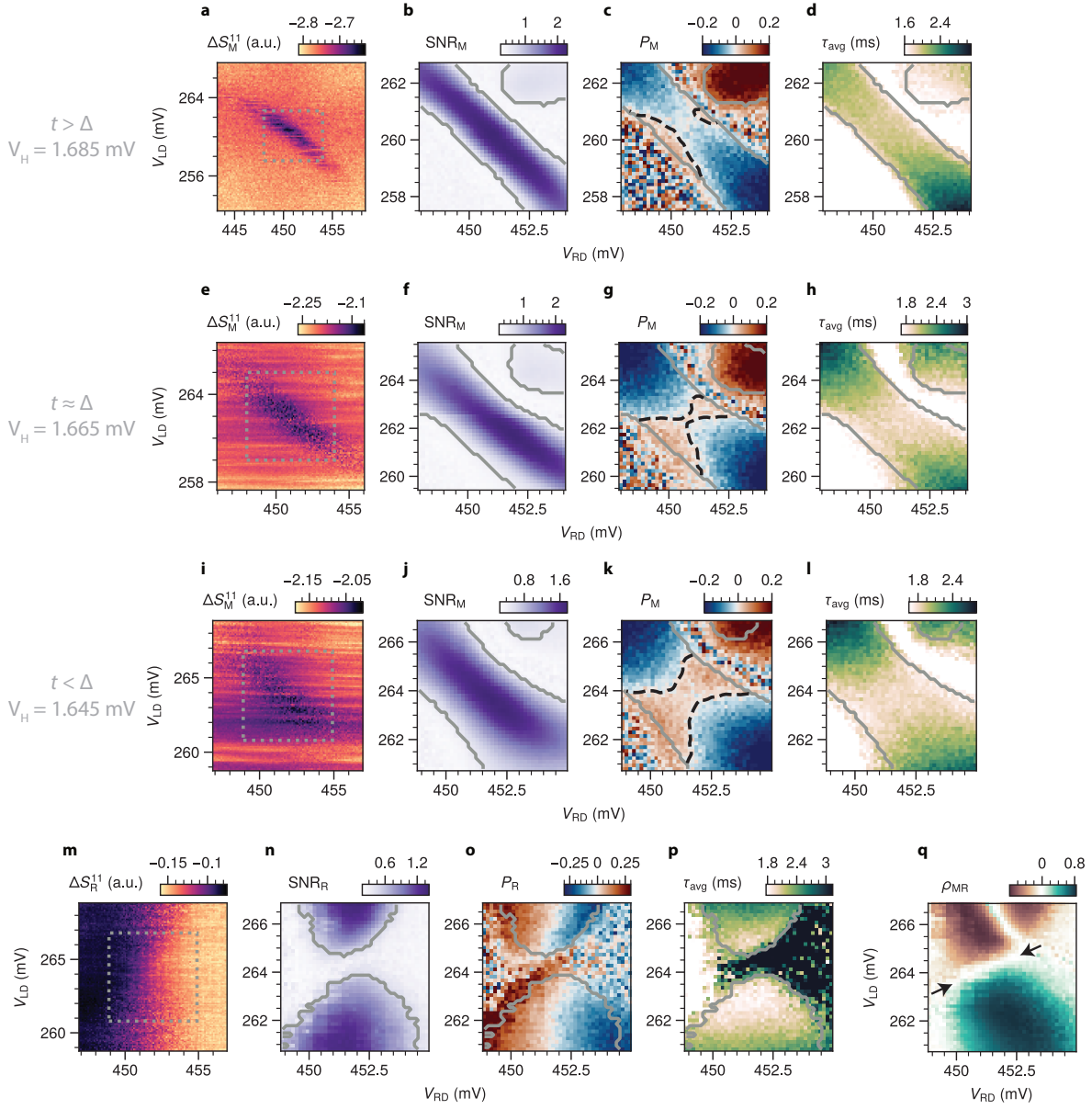


Fig. ED5 Evolution of charge-stability diagrams and switching behavior across the ECT-to-CAR transition. **a–d,** Measurements at $V_H = 1.685$ mV, where $t > \Delta$. The charge-stability diagram measured via quantum capacitance (**a**) shows strong signal along the detuning axis. The gray dotted box marks the region where 10 s time traces were measured to estimate (Methods section IV) the signal-to-noise ratio (SNR_M , panel **b**), parity polarization (P_M , panel **c**), and average switching time (τ_{avg} , panel **d**). In these panels, the gray contours indicate where $\text{SNR}_M = 0.5$. In panel **c**, a black dashed line highlights the contour where $P_M = 0$, calculated after applying a Gaussian filter with standard deviation of 1 pixel to reduce noise. This contour resembles an avoided crossing along the detuning axis, characteristic of the condition $t > \Delta$. **e–h,** Same measurements at $V_H = 1.665$ mV, where $t \approx \Delta$ near the Majorana sweet spot. In this case, the parity polarization map (panel **g**) shows no avoided crossing. Instead, regions of positive and negative parity polarization alternate around the center of the charge stability diagram, indicating that CAR and ECT are balanced. This is the dataset used in the main text. **i–l,** Same at $V_H = 1.645$ mV, where CAR dominates ($t < \Delta$). Here, the polarization map (panel **k**) shows that the avoided crossing reappears but now along the common-mode axis, reversing the pattern seen in **c**. This indicates that the system transitioned to a regime where $t < \Delta$. **m–p,** Corresponding data from panels **i–l** using the charge sensor, recorded via the right resonator. The SNR_R vanishes at the center of the charge-stability diagram, when the QDL is on resonance ($V_{LD} \approx 264$ mV). This indicates that a local charge measurement of QDR is not sufficient to determine the parity of the system. **q,** Map of the Pearson correlation coefficient ρ_{MR} between quantum capacitance and charge sensor signals in the $t < \Delta$ regime. The sign change of ρ_{MR} (black arrows) no longer follows a horizontal line. This is consistent with CAR dominating over ECT, as explained in more detail in Methods section VI.

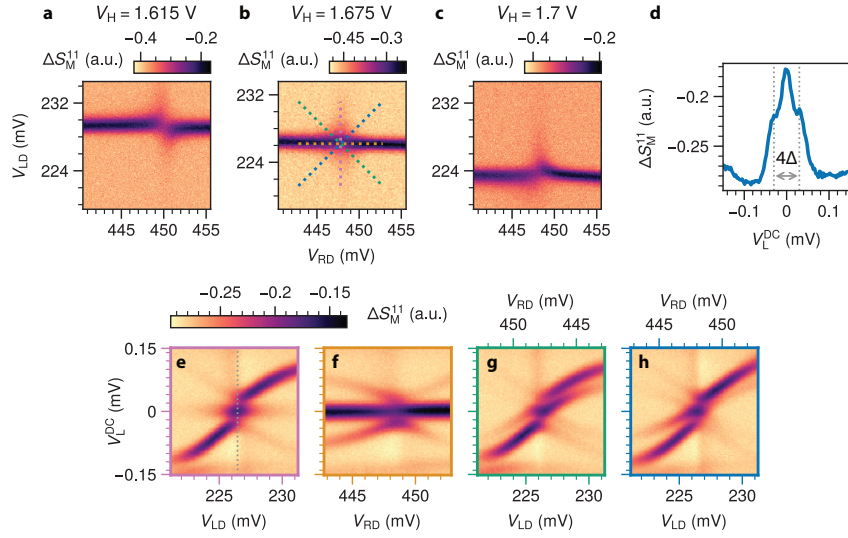


Fig. ED6 Transport measurement of the Majorana sweet spot using RF reflectometry. **a–c**, Zero-bias charge-stability diagrams for different values of V_H , used to tune the relative strength of elastic co-tunneling (ECT) and crossed Andreev reflection (CAR). In all panels, the left lead is operated as a tunnel probe, while the right side is blocked by the charge sensor. As a result, transport occurs predominantly through QDL, and visibility of the QDR resonance is suppressed. The orientation of the avoided crossing in panel **a** indicates that $t < \Delta$. As V_H increases, the avoided crossing first disappears when the sweet spot $t \approx \Delta$ (**b**) is approached. Further increasing V_H opens the avoided crossing in the opposite direction, indicating that $t > \Delta$ (**c**). The dotted lines in panel **b** indicate the axes along which the spectra of panels **e–h** were measured. **d**, Tunnel spectroscopy varying V_L^{DC} at the center of the charge-stability diagram of panel **b**. The spectrum exhibits a zero-bias peak separated from two excited states by a gap of $\approx 30 \mu\text{eV}$, consistent with MZMs in a minimal Kitaev chain. This linecut was extracted along the gray dotted line of panel **e**. **e, f**, Spectra measured while varying V_L^{DC} and the electrochemical potential of the left (**e**) or right (**f**) QD. The stable zero-bias peak indicates robustness against local perturbations. **g, h**, Spectra measured while varying V_L^{DC} and the electrochemical potential of both QDs along the common-mode (**g**) and detuning (**h**) axis. The zero-bias peak splits quadratically, illustrating limited protection against global perturbations.

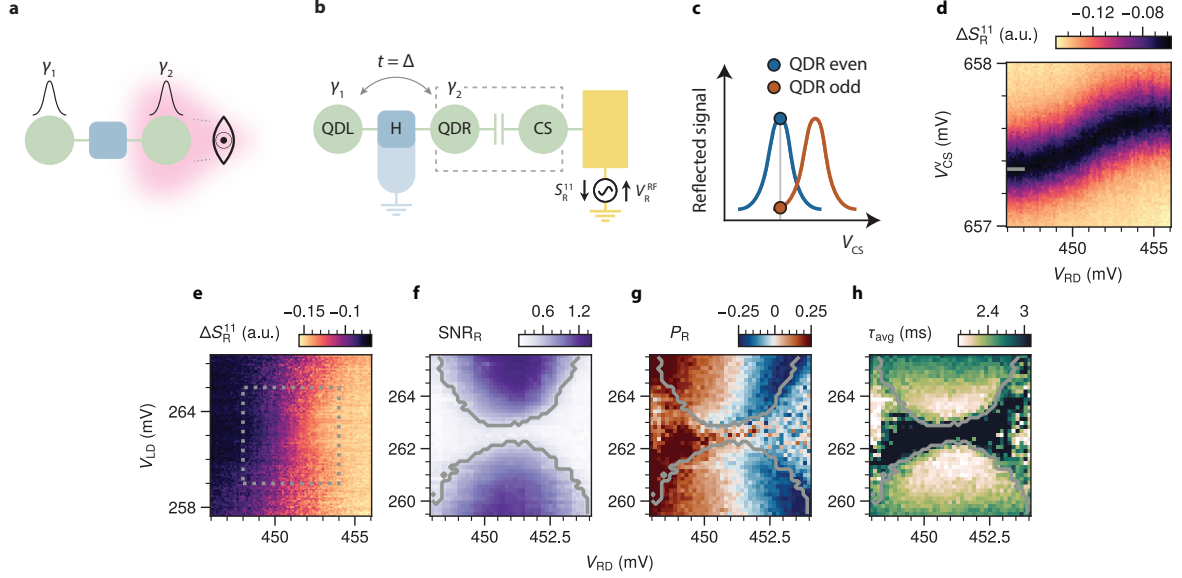


Fig. ED7 Parity readout using a local charge sensor. **a**, Illustration showing that a local probe coupled to only one MZM cannot access the joint parity $i\gamma_1\gamma_2$, and is thus insensitive to the stored quantum information **b**, Schematic of the charge sensing readout. A nearby quantum dot (CS) is capacitively coupled to QDR but isolated by a high tunnel barrier that prevents direct tunneling between them. A lead with a resonator is coupled to the CS for fast single-lead RF reflectometry [26]. **c**, Principle of charge sensing: changes in the charge on QDR alters the local electrostatic environment, shifting the CS resonance and modulating the reflected signal ΔS_R^{11} . **d**, Charge-stability diagram of QDR and CS measured via ΔS_R^{11} , with QDL held on resonance ($V_{LD} = 263$ mV). To correct for cross-capacitance, the voltage on V_{CS} is adjusted during V_{RD} sweeps, resulting in an effective compensated axis V_{CS}^V that is a linear combination of V_{RD} and V_{CS} . **e**, Charge-stability diagram of QDL and QDR with V_{CS}^V fixed (gray mark in panel **d**). Outside the QDL resonance, QDR shows fixed charge when its energy is above the hybrid gap E_{ABS} . Below this gap, parity switching is visible as signal noise. Near the QDL resonance ($V_{LD} = 263$ mV), the region of visible switching is reduced when QDL becomes lower in energy than QDR. **f–h**, The signal-to-noise ratio (SNR_R , panel **f**), parity polarization (P_R , panel **g**), and average switching time (τ_{avg} , panel **h**), obtained from time traces measured in the dotted gray box of panel **e**. In these panels, the gray contours indicate where $SNR_R = 0.5$. The SNR_R vanishes at the center of the diagram (where $V_{LD} \approx 262.5$ mV), indicating that a local probe cannot distinguish parity states of the system. This dataset was acquired simultaneously with the quantum capacitance measurements in Fig. 3e, and used to compute correlations in Fig. 4.

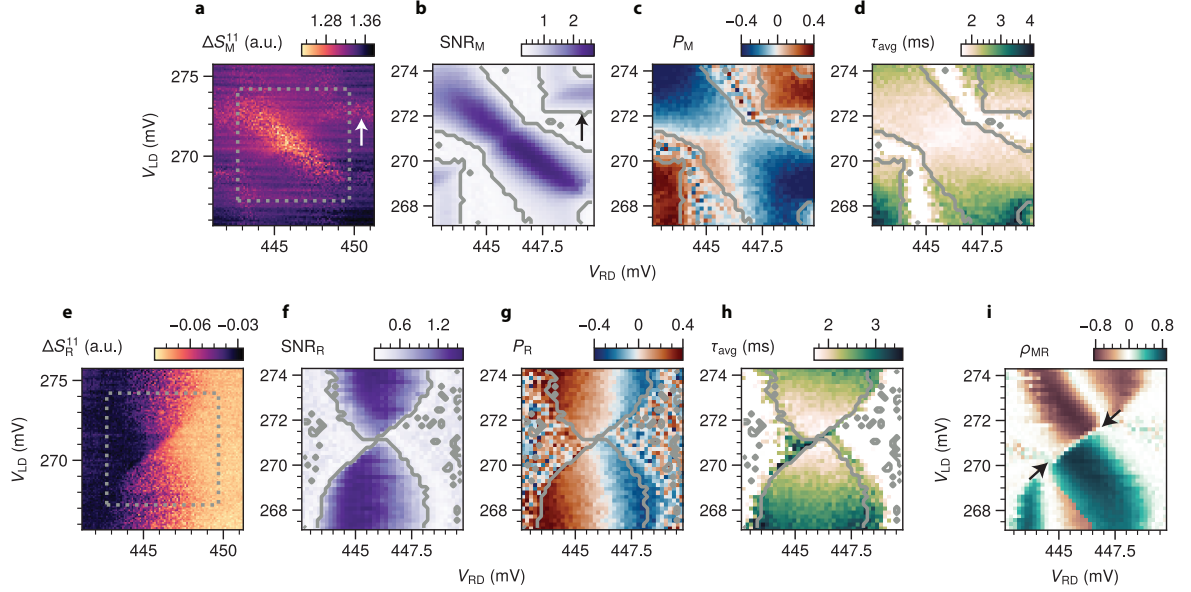


Fig. ED8 Time traces with weakly coupled QDs. **a–d**, Charge-stability diagram measured via quantum capacitance (panel **a**) in a weak interdot coupling regime ($V_H = 1.445$ V). The gray dotted box marks the region where time traces were measured to estimate the signal-to-noise ratio (SNR_M , panel **b**), parity polarization (P_M , panel **c**), and average switching time (τ_{avg} , panel **d**). We infer the weak coupling from the presence of signal when a QD is aligned to the lowest energy state in the hybrid, as highlighted by the arrows in panels **a, b** and discussed in Fig. 2. In these panels, the gray contours indicate where $\text{SNR}_M = 0.5$. The probing frequency for the middle resonator was 341 MHz instead of 340.8 MHz as in the rest of the text. The time traces in this figure were averaged in time bins of 200 μs (instead of 150 μs) to ensure that the averaging time is an exact multiple of inverse of the sampling rate (10 kHz). **e–h**, Same measurements via charge sensing. Charge-stability diagram of QDL and QDR (panel **e**). Outside the QDL resonance, QDR shows fixed charge when its energy is above the hybrid gap E_{ABS} . Below this gap, parity switching is visible as signal noise. Near the QDL resonance, the region of visible switching is reduced when QDL becomes lower in energy than QDR. The region where even and odd states are indistinguishable is narrower than in Fig. ED7 and Fig. ED9, consistent with small coupling between QDs (see Methods section VI). **i**, Pearson correlation coefficient between time traces measured with quantum capacitance and charge sensing. Similarly to Fig. ED5q, the transition region between positive and negative correlation (black arrows) is tilted. Additionally, this transition is more sharply defined, in line with the low coupling (see Methods section VI).

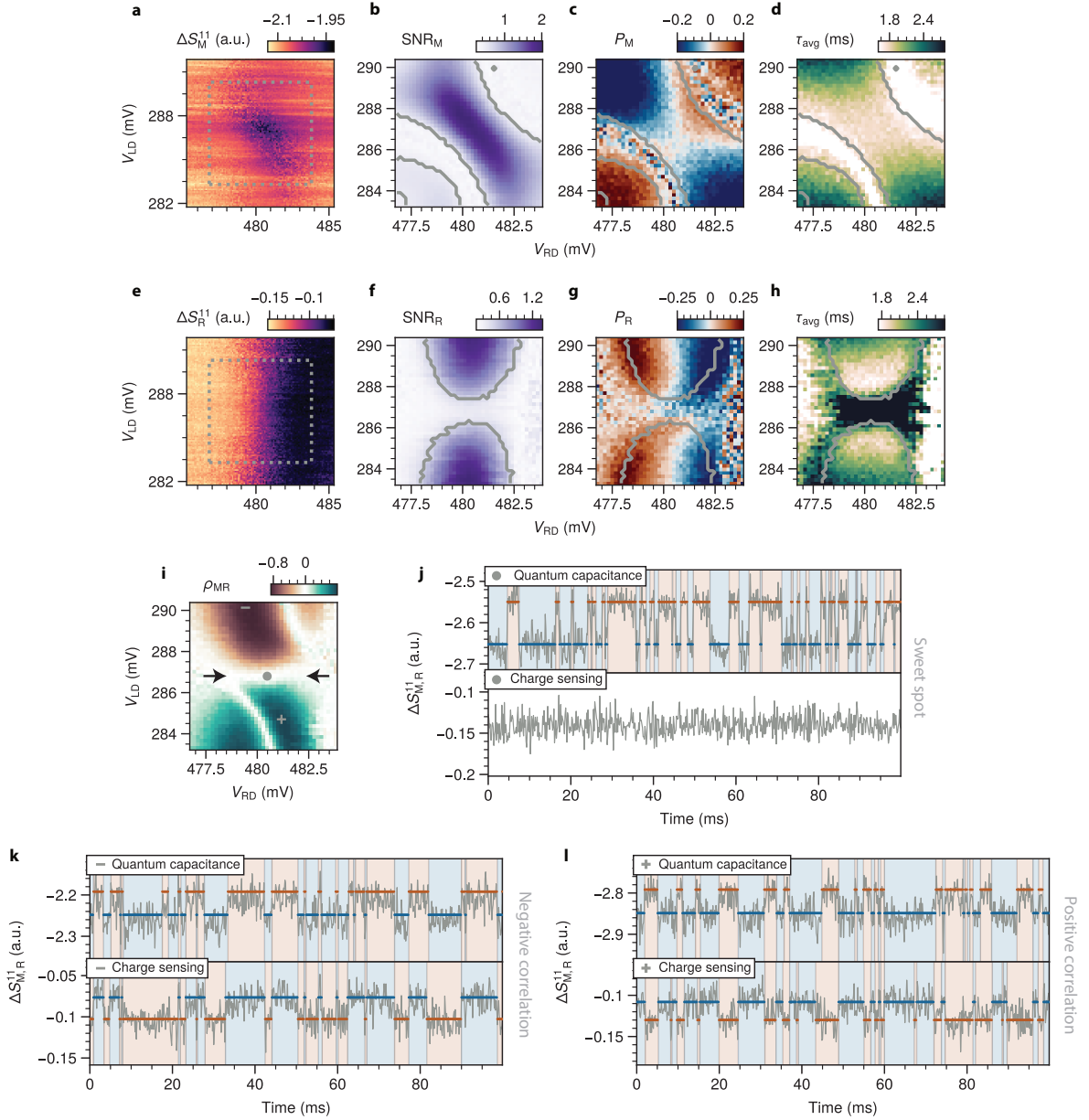


Fig. ED9 Majorana sweet spot reproduction with different QD resonances. **a–d**, Charge-stability diagram at $V_H = 1.625$ V measured via quantum capacitance (panel **a**), with the corresponding signal-to-noise ratio (SNR_M , panel **b**), parity polarization (P_M , panel **c**), and average switching time (τ_{avg} , panel **d**) for different QD resonances where $t \approx \Delta$. Panels **b–d** were measured inside the gray dotted box of panel **a**. In these panels, the gray contours indicate where $\text{SNR}_M = 0.5$. **e–h**, Same measurements via charge sensing. The charge-stability diagram of QDL and QDR is shown in panel **e**. Outside the QDL resonance, QDR shows fixed charge when its energy is above the hybrid gap E_{ABS} . Below this gap, parity switching is visible as signal noise. Near the QDL resonance ($V_{\text{LD}} = 286.8$ mV), the region of visible switching is reduced when QDL becomes lower in energy than QDR. The signal-to-noise ratio (SNR_R , panel **f**), parity polarization (P_R , panel **g**), and average switching time (τ_{avg} , panel **h**) are obtained from time traces measured in the dotted gray box of panel **e**. In these panels, the gray contours indicate where $\text{SNR}_R = 0.5$. The region where SNR_R vanishes near the center of the diagram is wider than for Fig. ED7 and Fig. ED8, indicating a stronger coupling. **i**, Pearson correlation coefficient between time traces measured with quantum capacitance and charge sensing. The black arrows indicate the region where the charge sensor is insensitive to parity switching events, resulting in vanishing correlation between time traces measured with quantum capacitance and charge sensing. Like for Fig. 4, this line is horizontal ($\mu_{\text{LD}} = 0$) which occurs only at the Majorana sweet spot ($t = \Delta$). **j–l**, Examples of uncorrelated (**j**), negatively correlated (**k**), and positively correlated (**l**) time traces. The marks in panel **i** indicate the specific gate values where these time traces were measured. Note that for panel **k** and **l** the reflected signal is, respectively, positively and negatively correlated, opposite to the state assignment (see Methods section V for more details).

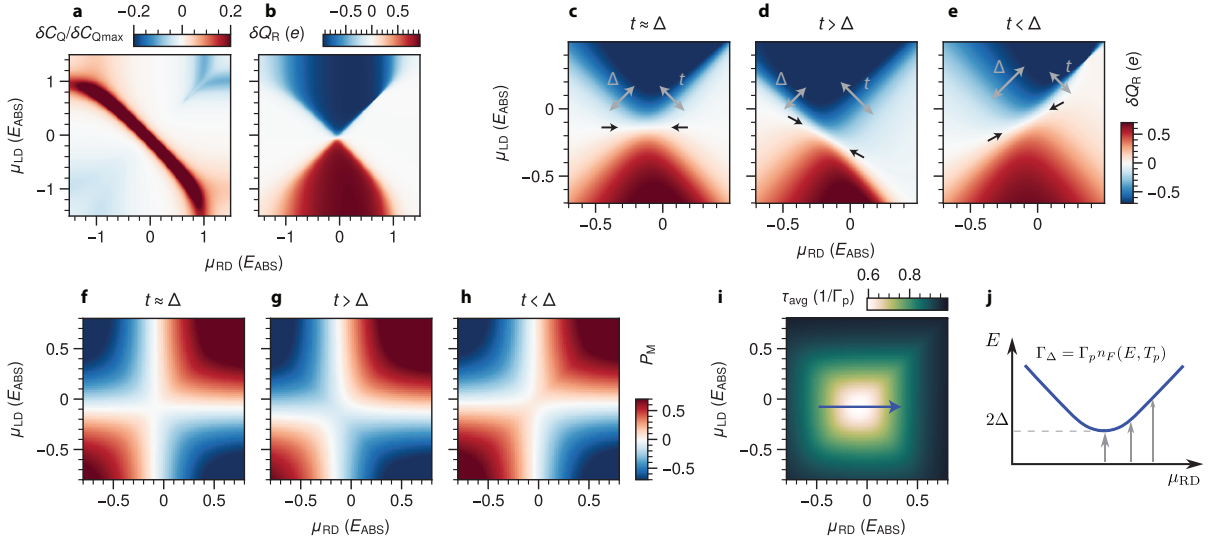


Fig. ED10 Theory model of quantum capacitance, charge sensing, and quasiparticle poisoning dynamics. **a,b,** Quantum capacitance (**a**) and right QD charge difference (**b**) for $t_L = t_R = 0.3E_{\text{ABS}}$, $\theta = \pi/8$, and $\mu_C = 0.75\Delta_P$, corresponding to a Majorana sweet spot. Red and blue areas indicate if the odd or even state yields the largest signal, and white where the states are indistinguishable. **c-e,** Zooms of QD charge difference with $t_L = t_R = 0.5E_{\text{ABS}}$, $\theta = \pi/8$, and $\mu_C = 0.75\Delta_P$ (**c**), $\mu_C = 2.5\Delta_P$ (**d**), and $\mu_C = 0.3\Delta_P$ (**e**). Here, various tilts of the $\mu_{\text{LD}} = \frac{\Delta-t}{\Delta+t}\mu_{\text{RD}}$ line are shown as emphasized by the black arrows. Gray arrows indicate the width of the transitions, set by Δ and t . **f-h,** Parity polarization maps for $t_L = t_R = 0.4E_{\text{ABS}}$, $\theta = \pi/8$, $T_p = 0.2\Delta_P$, with $\mu_C = 0.75\Delta_P$ (**f**), $\mu_C = 2.5\Delta_P$ (**g**), and $\mu_C = 0.3\Delta_P$ (**h**). These maps match the experimental behavior observed in Fig. ED5. **i,** Average parity lifetime $\tau_{\text{avg}} = 1/(\Gamma_{e \rightarrow o} + \Gamma_{o \rightarrow e})$ for same parameters as panel **f**. **j,** Schematic of the poisoning process, Γ_{Δ} , which decreases the lifetime in the center of **i** via poisoning to the excited states. The x-axis corresponds to the blue arrow in **i**. Details on the model can be found in Methods section VI, with calculations on the quantum capacitance and charge sensing signals in subsection A and state occupation in subsection B.

Methods

I Device fabrication

The device is fabricated using a modified shadow-wall lithography technique based on Refs [36, 37]. Additional fabrication details—including substrate preparation, nanowire surface treatment, superconductor growth, and ohmic contact fabrication—are described in Ref [37].

The base substrate consists of high-resistivity Si with a 100 nm Si_3N_4 layer grown via low-pressure chemical vapor deposition. Bottom gates (3 nm/7 nm Ti/Pd) were deposited by electron-beam evaporation, with 50 nm W bond pads added via RF sputtering. A 20 nm/10 nm $\text{Al}_2\text{O}_3/\text{HfO}_2$ gate dielectric was grown using atomic layer deposition.

To pattern the superconductor, a local shadow mask was created near the fine gate array. The substrate was first coated with PMMA (950k A8, ~ 800 nm thick), exposed using electron-beam lithography (EBL) (500×500 nm squares), and developed in MIBK:IPA (1:3). A 600 nm HSQ (FOX-25) layer was then spun on, baked, and patterned via EBL to define the superconductor openings. HSQ was developed in MF-21A at 50°C and PMMA removed in acetone, resulting in suspended masks supported by HSQ pillars.

The 95 nm diameter nanowire is placed using an optical nanomanipulator, followed by hydrogen-radical cleaning in an electron-beam evaporator. A 17.5 nm Al layer was deposited at a 30° angle to form a ~ 180 nm hybrid segment, then oxidized in 200 mtorr O_2 for 5 minutes. In Fig. ED2a, we show an example of a nanowire after deposition of the Al film, together with the shadow mask.

Following deposition, masks were mechanically removed. The same device after removal of the mask is shown in Fig. ED2b. To etch excess Al, PMMA (950k A4) was applied, vacuum-cured, and patterned via EBL to protect the hybrid section (see Fig. ED2c). The Al was etched using Transene type D (60 s at room temperature), rinsed in H_2O , and resist stripped in acetone. The result is shown in Fig. ED2d. Finally, ohmic contacts (10 nm/90 nm Cr/Au) were defined by EBL and deposited via electron-beam evaporation.

II Measurement setup

The sample was measured in an Oxford Triton-400 dilution refrigerator with a base temperature of ~ 20 mK, which is equipped with a 6/1/1 T vector magnet. The contacts to the nanowire are wire-bonded to LC resonators on a separate frequency-multiplexing chip [25]. The spiral inductors bonded to the superconductor and right lead have a nominal inductance of 570 nH and 150 nH, respectively. We use a Minicircuits ZUDC20-83-S+ directional coupler to couple the RF input and output lines. The reflected signal is first amplified via a Cosmic Microwave Tech CITLF3 high-electron-mobility transistor (HEMT) at the 4 K stage and additionally via a room temperature amplifier built in-house (M2j module for SPI

rack). RF signals are generated and demodulated using a Presto from Intermodulation Products. Infrared filters (XMA 2482-5002CL-CRYO), as well as several layers of shielding, are used to reduce noise and protect the sample from radiation that generates non-equilibrium quasiparticles in the superconducting film. Voltages applied to gate electrodes are controlled using digital to analog converters built in-house. Additionally, an arbitrary waveform generator built in-house (S5k module for SPI rack) is used to generate sawtooth signals for fast gate sweeps. If their frequency is much smaller than the bandwidth of the DC lines (limited by a second-order RC filter board with 1 kOhm resistors and 1 nF capacitors), they can be summed on top of the DC voltages for fast RF measurements. Two-dimensional measurement data is then obtained all at once (or line by line) instead of point by point, thus reducing the communication-time overhead. Averaging is performed to increase the quality of the signal. Fig. 2c, Fig. ED3, Fig. ED5a, Fig. ED6a–c and e–h were measured using the arbitrary waveform generator. Finally, we plot the response of the resonators in 2D measurements by projecting it onto the principal component axis. Further details of the fridge lines and circuitry can be found in Fig. ED1.

III Device tune-up

For tuning up the device, we follow a procedure that is described in ref [38]. The device is controlled using 11 bottom gates in a parallel magnetic field $B = 150$ mT. First, we perform transport measurements to check the device for Andreev bound states that reside in the hybrid segment, using V_{LT} and V_{RT} as tunnel barriers. Next, we form a pair of quantum dots adjacent to the hybrid by confining quantum levels around V_{RD} and V_{LD} with the adjacent gates. We proceed to increase their coupling to the hybrid by lowering the tunnel barrier between them using V_{LT} and V_{RT} , such that the quantum dot levels hybridize with the Andreev bound states. Next, we form the additional quantum dot on the right side that acts as the local charge sensor for QDR. We deplete the nanowire in between QDR and CS by setting $V_{cut,CS} = -1.2$ V while tracking the QDR and CS resonances. We subsequently take charge-stability diagrams of the QDs with V_{RD} and V_{LD} while adjusting V_H , to observe hybridization between the quantum dot levels and identify Majorana sweet spots. Finally, we deplete the left part of the nanowire using V_{cut} to isolate the chain from the left lead, while keeping track of QDL's resonance.

IV Time traces measurement and analysis

The time traces presented in this text are measured by continuously recording the complex demodulated reflected signal for 10 s, except for Fig. ED8, where we recorded 5 s time traces. The measurement bandwidth is 100 kHz for Fig. 3c,d and Fig. ED4c–g, 50 kHz for Fig. ED4a,b, 20 kHz for Fig. 3e, Fig. 4, Fig. ED5, Fig. ED7e–i, and Fig. ED9, and 10 kHz for Fig. ED8. We analyze each complex time trace by further averaging it in time bins of 150 μ s to improve the SNR, unless otherwise specified. Afterwards, we

project it onto the principal component axis. To unambiguously determine the principal component vector, we assume its real component to be positive. The resulting one-dimensional time trace is then split in 10 subtraces. We fit each subtrace with a two-state hidden Markov model using the Python package *hmmlearn*. The fitted Markov model assigns the most likely sequence of states to the data and estimates the transition probabilities between them. The two states are then mapped to the physical “even” and “odd” state as described in Methods section V. From the transition probabilities $p_{e \rightarrow o}, p_{o \rightarrow e}$ we calculate the corresponding transition rates as $\Gamma_{e \rightarrow o, o \rightarrow e} = -\log(1 - p_{o \rightarrow e, e \rightarrow o})/\tau_{\text{bin}}$. These can be used to estimate other relevant quantities such as the lifetimes $\tau_e = 1/\Gamma_{e \rightarrow o}$, $\tau_o = 1/\Gamma_{o \rightarrow e}$, $\tau_{\text{avg}} = 2/(\Gamma_{e \rightarrow o} + \Gamma_{o \rightarrow e})$ and the parity polarization $(\tau_e - \tau_o)/(\tau_e + \tau_o)$. Additionally, the average and standard deviation of the reflected signal can be used to estimate the center and width of the Gaussians shown in Fig. 3d. Finally, we average the results of each subtrace to estimate the corresponding quantities for the whole time trace. We consider the standard deviation of the mean as their uncertainty. Importantly, this analysis relies on the assumption that the switching processes are Poissonian [20]. To verify this, in Fig. ED4e we plot the distribution of the dwell times for the time trace discussed in Fig. 3c,d. The fit is in good agreement with an exponential distribution, as expected from a Poissonian process. Additionally, we note that the choice of integration time can affect the estimation of the parity lifetime, as shown in Fig. ED4f. Such a systematic error can occur if the integration time is not sufficiently smaller than the typical dwell time [39]. Using a shorter integration time would be detrimental for the SNR and state assignment, as shown in Fig. ED4c,d.

To further support our analysis, we extract the average switching time of the time trace in Fig. 3c,d using a different procedure that does not require averaging. We divide the unaveraged time trace in 10 subtraces and calculate the power spectral density of each subtrace, using Welch’s method as implemented in *scipy*. We fit each power spectral density using a Lorentzian with an additional background:

$$\text{PSD}(f) = 4A \frac{\Gamma_{\text{avg}}}{(2\Gamma_{\text{avg}})^2 + (2\pi f)^2} + B \quad (3)$$

In Fig. ED4g we plot the average power spectral density of the 10 subtraces. We obtain an average switching time of $\tau_{\text{avg}} = 1/\Gamma_{\text{avg}} = 1.51 \pm 0.07$ ms. This deviates by less than 0.5 ms from the estimation discussed in the main text. Although the finite integration time gives rise to a systematic error in the lifetime estimation, it does not affect the conclusions of the analysis.

Finally, we argue that the imperfect correlation coefficients presented in Fig. 4 can be attributed to suboptimal SNR. To simplify the analysis, we assume that the parity polarization does not significantly deviate from 0. Let X and Y be two telegraph processes whose values can be ± 1 . If they are perfectly correlated, their correlation is $\rho_{XY} = \langle XY \rangle = 1$. In the presence of assignment errors, the observed

signals are X_{obs} and Y_{obs} . If the assignment errors are uncorrelated and their probability is p_X and p_Y , the correlation is $\rho_{X_{obs}Y_{obs}} = \langle X_{obs}Y_{obs} \rangle = 1 - p_X - p_Y + 2p_Xp_Y$. For the positively correlated trace in Fig. 4, we extracted $\text{SNR}_M = 1.27$ and $\text{SNR}_R = 0.97$. The corresponding assignment error is $p_M = [1 - \text{erf}(\text{SNR}_M/\sqrt{2})]/2 \approx 0.10$ and $p_R \approx 0.17$, resulting in an expected correlation of $\rho_{MR} \approx 0.75$, close to measured value.

V State assignment

The two states of the Markov model are mapped to the physical “even” and “odd” state using the following procedures.

For the local charge sensing measurements we assume that the state is even at the left of the charge-stability diagram, where the measured dot is empty. We then use the same mapping for the full charge-stability diagram.

For the global quantum capacitance measurements, we assign the states such that the top-left and bottom-right corners of the charge-stability diagram are odd. This mapping is then used for the whole central region where the SNR is finite. In the regions with finite SNR that are disconnected from the central region (bottom-left and top-right of the charge-stability diagram), it is the odd state that gives rise to finite quantum capacitance, as further discussed in Methods section VI. Therefore, we invert the mapping for these regions. Practically, we identify the boundaries of the central region considering the contours $\text{SNR}_M = 0.5$. Beyond these contours, the inverted mapping is used. We include a padding of 3 pixels to account for small inaccuracies in the definition of the boundaries. Although the threshold choice is somewhat arbitrary, we find that if $\text{SNR}_M \lesssim 0.5$ the parity polarization varies significantly from pixel to pixel. This suggests that the analysis is not reliable if $\text{SNR}_M \lesssim 0.5$. The same holds for the charge sensing measurements.

VI Model

In this section we introduce a phenomenological model of the minimal Kitaev chain and quantum state dynamics, which we compare to experimental findings. First, we assume that the main contribution of CAR and ECT stems from an ABS state residing in the Al-covered part of the semiconductor, which we model as a proximitized resonant level. For simplicity, we neglect the rest of the superconducting continuum similar to Refs. [38, 40]. This results in the following QD-ABS-QD Hamiltonian,

$$H = H_{QD} + H_{ABS} + H_T, \quad (4)$$

$$H_{QD} = -\mu_{LD}d_L^\dagger d_L - \mu_{RD}d_R^\dagger d_R, \quad (5)$$

$$H_{ABS} = -\mu_C \sum_{\sigma} d_{C\sigma}^{\dagger} d_{C\sigma} + \Delta_P \left(d_{C\uparrow}^{\dagger} d_{C\downarrow}^{\dagger} + d_{C\downarrow} d_{C\uparrow} \right) \quad (6)$$

$$H_T = \sum_{j=L/R} \left[t_{j\uparrow} d_j^{\dagger} d_{C\uparrow} + t_{j\downarrow} d_j^{\dagger} d_{C\downarrow} + \text{h.c.} \right]. \quad (7)$$

Here, d_L and d_R are annihilation operators for the spin-polarized left/right QDs, and $d_{C\sigma}$ for the central spin-full resonant level which is proximitized with superconducting pairing Δ_P . A small Zeeman splitting is expected for the resonant level, as it is partly screened by the superconductor, which we for simplicity neglect in this analysis [40]. Chemical potentials are given by μ_{LD} , μ_{RD} , and μ_C . Now, by performing a Bogoliubov transformation, $d_{C\uparrow} = u\beta_{\uparrow} - v\beta_{\downarrow}^{\dagger}$ and $d_{C\downarrow} = u\beta_{\downarrow} + v\beta_{\uparrow}^{\dagger}$, we obtain,

$$H_{ABS} = E_{ABS} \sum_{\sigma} \beta_{\sigma}^{\dagger} \beta_{\sigma}, \quad (8)$$

$$H_T = \sum_{j=L/R} \left[t_{j\uparrow} d_j^{\dagger} (u\beta_{\uparrow} - v\beta_{\downarrow}^{\dagger}) + t_{j\downarrow} d_j^{\dagger} (u\beta_{\downarrow} + v\beta_{\uparrow}^{\dagger}) + \text{h.c.} \right], \quad (9)$$

where $E_{ABS} = \sqrt{\mu_C^2 + \Delta_P^2}$ is the effective gap of the ABS, and $u = \frac{1}{\sqrt{2}} \frac{-\Delta_P/E_{ABS}}{\sqrt{1-\mu_C/E_{ABS}}}$ and $v = \frac{1}{\sqrt{2}} \sqrt{1-\mu_C/E_{ABS}}$ are the coherence factors. The tunneling, $t_{j\sigma}$, contains spin-dependence due to spin-orbit interaction. Assuming that both left and right QDs are spin-polarized in the down direction, $d_L = d_{L\downarrow}$, then $t_{L\downarrow}$ denotes normal tunneling and $t_{L\uparrow}$ spin-flipping tunneling. Next, to obtain the typical minimal Kitaev chain Hamiltonian we use quasi-degenerate perturbation theory to trace out the ABS levels and find

$$H_0 = H_{QD} + \Delta d_L^{\dagger} d_R^{\dagger} + t d_L^{\dagger} d_R + \text{h.c.}, \quad (10)$$

$$\Delta = -\frac{2uv}{E_{ABS}} (t_{L\uparrow} t_{R\downarrow} - t_{L\downarrow} t_{R\uparrow}), \quad (11)$$

$$t = \frac{u^2 - v^2}{E_{ABS}} (t_{L\uparrow} t_{R\uparrow} + t_{L\downarrow} t_{R\downarrow}), \quad (12)$$

which is valid for $|E_{ABS} \pm \mu_j| \ll |t_{j\sigma}|$ for $j = L/R$. To obtain the MZM sweet spot from this model, we require $|t| = |\Delta|$ which is fulfilled by $2uv = \pm (t_{L\uparrow} t_{R\uparrow} + t_{L\downarrow} t_{R\downarrow}) / t_L t_R$ with $t_j = \sqrt{t_{j\uparrow}^2 + t_{j\downarrow}^2}$. This yields a gap to the excited states at the sweet spot

$$2|\Delta| = \frac{2t_L t_R}{E_{ABS}} |2uv (u^2 - v^2)| = \frac{t_L t_R}{E_{ABS}} |\sin 4\theta|, \quad (13)$$

at chemical potentials $\mu_{LD} = t_L^2 \frac{u^2 - v^2}{E_{ABS}}$ and $\mu_{RD} = t_R^2 \frac{u^2 - v^2}{E_{ABS}}$. In the last expression, the angle θ connects to the tunnel couplings in the following way; $t_{L\uparrow} = t_L \cos \theta$, $t_{R\uparrow} = t_R \cos \theta$, $t_{L\downarrow} = t_L \sin \theta$, $t_{R\downarrow} = -t_R \sin \theta$, and the gap is maximized if $\theta = \pi/8$. In general however, the ratios $t_{j\uparrow}/t_{j\downarrow}$, and therefore

θ , are geometrically set in experiment and not gate-tuneable. The primary strategy is therefore to tune μ_C via electrostatic gating, which tunes u and v , until a sweet spot is observed [5]. In general, both the full Hamiltonian (Eq. 4) and the minimal Kitaev Hamiltonian, (Eq. 10) can be separated into even and odd parity sectors, with E_{en} and E_{on} denoting the n th excitation in the respective parity sector. For the Kitaev model, the lowest energy states in each parity are given by $E_{e0} = \delta - \sqrt{\delta^2 + \Delta} \equiv E_e^-$ and $E_{o0} = \delta - \sqrt{\varepsilon^2 + t^2} \equiv E_o^-$, where $\delta = (\mu_{LD} + \mu_{RD})/2$ and $\varepsilon = (\mu_{LD} - \mu_{RD})/2$, with excited states at $E_{e1} = 2\delta - E_{e0}$ and $E_{o1} = 2\delta - E_{o0}$, which are used in the main text. The theory plots shown in the paper are made by diagonalizing Eq. 4 to ensure that details of the ABS beyond perturbation are captured, while Eq. 10 is used to derive minimal equations and gain intuition from the results.

A Quantum capacitance and charge sensing

In this subsection, we focus on the primary measures used in the experiment, namely the signals from quantum capacitance measured on the superconducting lead, and charge sensing of the right quantum dot. To derive the quantum capacitance arising from a small oscillating voltage V_S on the superconductor, we ask how the energy of state n changes with small fluctuations δV_S . Expanding to second order, we get

$$E_n(V_S + \delta V_S) \approx E_n(V_S) + E'_n(V_S)\delta V_S + \frac{1}{2}E''_n(V_S)(\delta V_S)^2 \quad (14)$$

$$= \frac{1}{2}E''_n(V_S) \left(\delta V_S + \frac{E'_n(V_S)}{E''_n(V_S)} \right)^2 + E_n(V_S) - \frac{1}{2} \frac{E'_n(V_S)^2}{E''_n(V_S)}, \quad (15)$$

where in the second line we recognize $C_n = E''_n(V_S)$ as a capacitance, as it matches the quadratic response $E_C = 1/2C\delta V^2$ of a regular capacitor [41]. We note that this yields the capacitive response of a given state n in a closed system, but neglects responses arising from opening the system to a bath, such as decoherence or change of state [42]. We consider this appropriate as poisoning is slow compared to quantum capacitance measurements. Next, to evaluate E''_n , we consider the effects of δV_S on chemical potentials,

$$\mu_j(V_S + \delta V_S) \approx \mu_j(V_S) + (\alpha_{jS} - 1)e\delta V_S, \quad (16)$$

where we subtracted $e\delta V_S$ since we measure chemical potentials relative to the superconductor, and with α_{jS} specifying the lever arm to the superconductor. For the ABS we set $\alpha_{CS} = 1$ as we assume a strong capacitive coupling to the superconducting lead, thus fixing its chemical potential to the superconductor.

For the QDs, $\alpha_{LS}, \alpha_{RS} \neq 1$, as the bottom gates primarily set their chemical potential. As such, we obtain

$$E_n'' \approx \frac{e^2}{8}(2 - \alpha_{LS}^2 - \alpha_{RS}^2) \frac{d^2 E_n}{d\delta^2} - \frac{e^2}{8}(\alpha_{LS}^2 - \alpha_{RS}^2) \frac{d^2 E_n}{d\varepsilon^2}, \quad (17)$$

Finally, assuming that lever arms are fairly symmetrical ($\alpha_{LS} \approx \alpha_{RS}$) and defining $\alpha^2 = 1 - \alpha_{LS}^2$, we use the Hellmann-Feynman theorem to rewrite

$$E_n''(V_S) \approx \frac{\alpha^2 e^2}{4} \frac{d^2 E_n}{d\delta^2} = \frac{\alpha^2 e^2}{4} \frac{d}{d\delta} \langle n | \frac{dH}{d\delta} | n \rangle. \quad (18)$$

Here, $dH/d\delta$ is simply the total charge of both QDs (see Eq. 4), and we arrive at the quantum capacitance of state n

$$C_n \approx \frac{\alpha^2 e^2}{4} \frac{d^2 E_n}{d\delta^2} = -\frac{\alpha^2 e^2}{2} \frac{\partial}{\partial \delta} \langle n | d_L^\dagger d_L + d_R^\dagger d_R | n \rangle. \quad (19)$$

Using this equation for the minimal Hamiltonian (Eq. 10), the quantum capacitance of the odd states is zero, as both are superpositions of $|01\rangle$ and $|10\rangle$ with a constant total charge of 1. The even ground state yields a signal

$$C_{e0} = -\alpha^2 e^2 \frac{1}{4} \frac{\Delta^2}{(\delta^2 + \Delta^2)^{\frac{3}{2}}}, \quad (20)$$

corresponding to a minimum around $\delta \approx 0$ of width Δ . We note that $\alpha_{LS} \neq \alpha_{RS}$ would also yield a signal for the odd state along the line $\varepsilon \approx 0$ of width t . This is not observed in the experiment, supporting our assumption of $\alpha_{LS} \approx \alpha_{RS}$. In Fig. ED10a, we plot the quantum capacitance signal in terms of the difference $\delta C_Q = C_{o0} - C_{e0}$, which is appropriate as both C_{e0} and C_{o0} are strictly negative for Eq. 4 due to QD charge monotonically increasing with δ in Eq. 19. This quantity thus shows which state yields the dominant quantum capacitance signal, while areas of $\delta C_Q = 0$ indicate where the states are indistinguishable, i.e. yielding signals of equal amplitude. The positive signal along the anti-diagonal $\mu_{LD} \approx -\mu_{RD}$ stems from Eq. 20, while the negative corners stem from the odd state hybridizing with the Andreev bound state when $E_{\text{ABS}} \approx E_{o0} - E_{e0}$, which goes beyond the minimal Kitaev chain Hamiltonian.

For charge sensing, it is the charge of the right quantum dot that is measured, which for state n is given by

$$Q_{R,n} = \langle n | d_R^\dagger d_R | n \rangle. \quad (21)$$

For the minimal Kitaev Hamiltonian, Eq. 10, this yields the signals

$$Q_{R,e0} = \frac{\Delta^2}{2\sqrt{\delta^2 + \Delta^2}} \frac{1}{\sqrt{\delta^2 + \Delta^2} + \delta}, \quad Q_{R,o0} = \frac{t^2}{2\sqrt{\varepsilon^2 + t^2}} \frac{1}{\sqrt{\varepsilon^2 + t^2} + \varepsilon}, \quad (22)$$

These quantities are strictly positive and describe an anti-diagonal and diagonal line, respectively, separating plateaus of $Q_R = 1$ from $Q_R = 0$. Subtracting the lines ($\delta Q_R = Q_{R,o0} - Q_{R,e0}$) yields two characteristic triangular shapes as shown in Fig. ED10b. To identify the line of indistinguishability via charge sensing, we look for the condition

$$Q_{R,e0} = Q_{R,o0} \Rightarrow \Delta \left(\sqrt{\varepsilon^2 + t^2} + \varepsilon \right) = t \left(\sqrt{\delta^2 + \Delta^2} + \delta \right), \quad (23)$$

which is fulfilled by $\mu_{LD} = \frac{\Delta-t}{\Delta+t}\mu_{RD}$. This can be verified by using the corresponding relations $\delta = \Delta\mu_{RD}/(\Delta+t)$ and $\varepsilon = t\mu_{RD}/(\Delta+t)$ in Eq. 23. This equation yields an indicator for the sweet spot, as the criterion of $t = \Delta$ yields a flat line separating the triangles, while other choices yields a tilted line (Fig. ED10c-e). This slope also correlates to the width of the δQ_R transitions, where the anti-diagonal width is given by Δ and the diagonal by t , meaning that the line tilts towards the diagonal of lowest width. Focusing now on the sweet spot ($\Delta = t$), we expand δQ_R around μ_{LD}/Δ for $\mu_{RD} = 0$, yielding

$$\delta Q_R \approx \frac{-16\Delta\mu_{LD}}{16\Delta^2 + \mu_{LD}^2}, \quad (24)$$

which corresponds to a Lorentzian with a full width at half maximum of 2Δ . The width of the white indistinguishability line separating the tips of the two triangles in Fig. ED10c can thus be used to estimate the size of the gap at the sweet spot.

B Occupation

Above, we investigated the minimal Hamiltonian and the signals arising from the lowest-energy parity states. Next, we wish to tackle the occupation of the even and odd parity states which goes beyond the closed-system Hamiltonian in Eq. 4, and provide a minimal description for the observed parity polarizations and parity lifetimes. First, changing parity requires the addition or removal of a quasiparticle from the QD-ABS-QD system, which we assume to be the slowest rate in the system providing the millisecond parity lifetimes. Accordingly, we assume that the intra-parity relaxation rate is much faster [30], such that the system reaches the lowest-energy state in a given parity sector (E_{e0} for even and E_{o0} for odd) between parity switching events. We thus concentrate solely on the parity-changing rates which we assume to follow Fermi rates

$$\Gamma_{e \rightarrow o} = \Gamma_p n_F(E_{e0} - E_{o0}, T_p) + \Gamma_p n_F(E_{e0} - E_{o1}, T_p), \quad (25)$$

$$\Gamma_{o \rightarrow e} = \Gamma_p n_F(E_{o0} - E_{e0}, T_p) + \Gamma_p n_F(E_{o0} - E_{e1}, T_p). \quad (26)$$

Here, Γ_p denotes the rate of poisoning quasiparticles that change the systems parity, $n_F(E, T) = 1/(1 + \exp E/k_B T_p)$ the fermi distribution, and T_p a phenomenological temperature added to capture smoothness of the parity polarization maps. This modeling is motivated by three observational facts: First, the parity polarizes towards the lowest-energy parity (specifically, towards even parity when $E_{e0} < E_{o0}$ and odd parity otherwise), as seen in Fig. 3 of the main text. Second, the reflected signals S_M^{11} and S_R^{11} shows only signal from two states, meaning higher energy states than E_{e0} and E_{o0} are only negligibly occupied. Third, parity lifetimes decrease towards the central degeneracy point where the gap is lowest, as seen in Fig. ED5. This indicates that the excited states E_{e1} and E_{o1} are involved in poisoning processes.

From this model, the probabilities of being in the even and odd state are given by $P_e = \Gamma_{o \rightarrow e}/(\Gamma_{e \rightarrow o} + \Gamma_{o \rightarrow e})$ and $P_o = \Gamma_{e \rightarrow o}/(\Gamma_{e \rightarrow o} + \Gamma_{o \rightarrow e})$, with polarization given by $P_M = P_e - P_o$ which is plotted in Fig. ED10f-h for different values of t and Δ . The opening and closing of the cross mimics that of spectroscopy and corresponds to experiments shown in Fig. ED5. In total, these equations mimic the system being coupled to a metallic bath with rate Γ_p and temperature T_p . However, this does not result in a thermal equilibrium distribution at T_p due to the assumption of fast intra-parity relaxation, such that only the lowest-energy parity states are populated. For $T_p \rightarrow 0$ the system polarizes completely in the lowest energy parity sector, with constant $\Gamma_{e \rightarrow o} + \Gamma_{o \rightarrow e} = \Gamma_p$. In the other limit of $k_B T_p \gg 2\Delta$, a peak in $\Gamma_{e \rightarrow o} + \Gamma_{o \rightarrow e} \approx 2\Gamma_p$ occurs at the sweet spot, corresponding to a dip in τ_{avg} as shown in Fig. ED10i. This is due to the added transitions, $\Gamma_\Delta = \Gamma_p n_F(E_{e0} - E_{o1}, T)$ (and $e \leftrightarrow o$), to the excited states, which at the vicinity of the sweet spot are minimal, $E_{e1} - E_{e0} \approx 2\Delta$ and $E_{o0} - E_{o1} \approx 2\Delta$, as sketched in Fig. ED10j. Lastly, using this model we can also calculate the average quantum capacitance given by $\langle C \rangle = P_e C_{e0} + P_o C_{o0}$, which for small coupling is plotted in Fig. 2d of the main text.

References

- [1] Kitaev, A. Y. Unpaired Majorana fermions in quantum wires. *Physics-uspekhi* **44**, 131 (2001).
- [2] Kitaev, A. Y. Fault-tolerant quantum computation by anyons. *Annals of physics* **303**, 2–30 (2003).
- [3] Nayak, C., Simon, S. H., Stern, A., Freedman, M. & Das Sarma, S. Non-Abelian anyons and topological quantum computation. *Reviews of Modern Physics* **80**, 1083–1159 (2008).
- [4] Sarma, S. D., Freedman, M. & Nayak, C. Majorana zero modes and topological quantum computation. *npj Quantum Information* **1**, 1–13 (2015).
- [5] Dvir, T. *et al.* Realization of a minimal Kitaev chain in coupled quantum dots. *Nature* **614**, 445–450 (2023).
- [6] ten Haaf, S. L. *et al.* A two-site Kitaev chain in a two-dimensional electron gas. *Nature* **630**, 329–334 (2024).
- [7] Sau, J. D. & Sarma, S. D. Realizing a robust practical Majorana chain in a quantum-dot-superconductor linear array. *Nature communications* **3**, 964 (2012).
- [8] Leijnse, M. & Flensberg, K. Parity qubits and poor man’s Majorana bound states in double quantum dots. *Physical Review B* **86**, 134528 (2012).
- [9] Liu, C.-X., Pan, H., Setiawan, F., Wimmer, M. & Sau, J. D. Fusion protocol for Majorana modes in coupled quantum dots. *Physical Review B* **108**, 085437 (2023).
- [10] Boross, P. & Pályi, A. Braiding-based quantum control of a Majorana qubit built from quantum dots. *Physical Review B* **109**, 125410 (2024).
- [11] Tsintzis, A., Souto, R. S., Flensberg, K., Danon, J. & Leijnse, M. Majorana qubits and non-abelian physics in quantum dot-based minimal Kitaev chains. *PRX Quantum* **5**, 010323 (2024).
- [12] Seoane Souto, R. & Aguado, R. *Subgap states in semiconductor-superconductor devices for quantum technologies: Andreev qubits and minimal Majorana chains*, 133–223 (Springer Nature Switzerland, 2024).
- [13] Bonderson, P., Freedman, M. & Nayak, C. Measurement-only topological quantum computation. *Physical Review Letters* **101**, 010501 (2008).

- [14] Vijay, S. & Fu, L. Teleportation-based quantum information processing with Majorana zero modes. *Physical Review B* **94**, 235446 (2016).
- [15] Plugge, S., Rasmussen, A., Egger, R. & Flensberg, K. Majorana box qubits. *New Journal of Physics* **19**, 012001 (2017).
- [16] Steiner, J. F. & von Oppen, F. Readout of Majorana qubits. *Physical Review Research* **2**, 033255 (2020).
- [17] Rainis, D. & Loss, D. Majorana qubit decoherence by quasiparticle poisoning. *Physical Review B* **85**, 174533 (2012).
- [18] Aumentado, J., Keller, M. W., Martinis, J. M. & Devoret, M. H. Nonequilibrium Quasiparticles and $2e$ Periodicity in Single-Cooper-Pair Transistors. *Physical Review Letters* **92**, 066802 (2004).
- [19] Catelani, G., Schoelkopf, R. J., Devoret, M. H. & Glazman, L. I. Relaxation and frequency shifts induced by quasiparticles in superconducting qubits. *Physical Review B* **84**, 064517 (2011).
- [20] Hays, M. *et al.* Direct Microwave Measurement of Andreev-Bound-State Dynamics in a Semiconductor-Nanowire Josephson Junction. *Physical Review Letters* **121**, 047001 (2018).
- [21] Karzig, T., Cole, W. S. & Pikulin, D. I. Quasiparticle Poisoning of Majorana Qubits. *Physical Review Letters* **126**, 057702 (2021).
- [22] Aghaee, M. *et al.* Interferometric single-shot parity measurement in InAs–Al hybrid devices. *Nature* **638**, 651–655 (2025).
- [23] Contamin, L. C., Delbecq, M. R., Douçot, B., Cottet, A. & Kontos, T. Hybrid light-matter networks of Majorana zero modes. *npj Quantum Information* **7**, 1–9 (2021).
- [24] Badawy, G. *et al.* High Mobility Stemless InSb Nanowires. *Nano Letters* **19**, 3575–3582 (2019).
- [25] Hornibrook, J. M. *et al.* Frequency multiplexing for readout of spin qubits. *Applied Physics Letters* **104**, 103108 (2014).
- [26] Persson, F., Wilson, C., Sandberg, M., Johansson, G. & Delsing, P. Excess dissipation in a single-electron box: The Sisyphus resistance. *Nano letters* **10**, 953–957 (2010).
- [27] Bruhat, L. *et al.* Cavity Photons as a Probe for Charge Relaxation Resistance and Photon Emission in a Quantum Dot Coupled to Normal and Superconducting Continua. *Physical Review X* **6**, 021014

- (2016).
- [28] van Driel, D. *et al.* Charge sensing the parity of an Andreev molecule. *PRX Quantum* **5**, 020301 (2024).
 - [29] Vigneau, F. *et al.* Probing quantum devices with radio-frequency reflectometry. *Applied Physics Reviews* **10** (2023).
 - [30] Petta, J. R., Johnson, A. C., Marcus, C. M., Hanson, M. P. & Gossard, A. C. Manipulation of a Single Charge in a Double Quantum Dot. *Physical Review Letters* **93**, 186802 (2004).
 - [31] Nguyen, H. Q. *et al.* Electrostatic control of quasiparticle poisoning in a hybrid semiconductor-superconductor island. *Phys. Rev. B* **108**, L041302 (2023).
 - [32] Hinderling, M. *et al.* Flip-chip-based fast inductive parity readout of a planar superconducting island. *PRX Quantum* **5**, 030337 (2024).
 - [33] Luethi, M., Legg, H. F., Loss, D. & Klinovaja, J. From perfect to imperfect poor man’s Majoranas in minimal Kitaev chains. *Physical Review B* **110**, 245412 (2024).
 - [34] Pan, H., Das Sarma, S. & Liu, C.-X. Rabi and Ramsey oscillations of a Majorana qubit in a quantum dot-superconductor array. *Physical Review B* **111**, 075416 (2025).
 - [35] Wesdorp, J. *et al.* Dynamical polarization of the fermion parity in a nanowire Josephson junction. *Physical Review Letters* **131**, 117001 (2023).
 - [36] Heedt, S. *et al.* Shadow-wall lithography of ballistic superconductor–semiconductor quantum devices. *Nature Communications* **12**, 4914 (2021).
 - [37] Mazur, G. P. *et al.* Spin-mixing enhanced proximity effect in aluminum-based superconductor–semiconductor hybrids. *Advanced Materials* **34**, 2202034 (2022).
 - [38] Zatelli, F. *et al.* Robust poor man’s Majorana zero modes using Yu-Shiba-Rusinov states. *Nature Communications* **15**, 7933 (2024).
 - [39] Naaman, O. & Aumentado, J. Poisson Transition Rates from Time-Domain Measurements with a Finite Bandwidth. *Physical Review Letters* **96**, 100201 (2006).
 - [40] Liu, C.-X., Wang, G., Dvir, T. & Wimmer, M. Tunable superconducting coupling of quantum dots via Andreev bound states in semiconductor-superconductor nanowires. *Physical Review Letters* **129**,

267701 (2022).

- [41] Secchi, A. & Troiani, F. Theory of multidimensional quantum capacitance and its application to spin and charge discrimination in quantum dot arrays. *Physical Review B* **107**, 155411 (2023).
- [42] Peri, L., Benito, M., Ford, C. J. & Gonzalez-Zalba, M. F. Unified linear response theory of quantum electronic circuits. *npj Quantum Information* **10**, 114 (2024).